4 From Magma Source to Volcanic Sink Under Tagoro Volcano (El Hierro, Canary Islands): Petrologic, Geochemical and Physiographic Evolution of the 2011–2012 Submarine Eruption

Antonio M. Álvarez-Valero, Olga Sánchez-Guillamón, Irene Navarro, Helena Albert, Antonio Polo Sánchez, José A. Lozano Rodríguez, Adelina Geyer, Joan Martí, Masao Ban, María Gómez-Ballesteros, Manuel Catalán, Natalia García, Eugenio Fraile-Nuez, Ramón Casillas, María C. Martín-Luis, Desirée Palomino, Juan T. Vázquez, Nieves López-González, Daniel Hernández-Barreña, and Elena Núñez-Guerrero

A. M. Álvarez-Valero (✉) · I. Navarro · A. P. Sánchez · N. García · D. Hernández-Barreña · E. Núñez-Guerrero
Departamento de Geología, Universidad de Salamanca, 37008 Salamanca, Spain
e-mail: aav@usal.es

O. Sánchez-Guillamón · D. Palomino · J. T. Vázquez · N. López-González
Instituto Español de Oceanografía (IEO-CSIC), Centro Oceanográfico de Málaga, 29640 Fuengirola, Spain

H. Albert
Departamento de Mineralogía, Petrología y Geología Aplicada, Universidad de Barcelona, 08028 Barcelona, Spain

J. A. L. Rodríguez · E. Fraile-Nuez
Instituto Español de Oceanografía (IEO-CSIC), Centro Oceanográfico de Canarias, 38180 Santa Cruz de Tenerife, Spain

A. Geyer · J. Martí
Geosciences Barcelona—CSIC, 08028 Barcelona, Spain

M. Ban
Faculty of Science, Yamagata University, Yamagata, Japan

M. Gómez-Ballesteros
Instituto Español de Oceanografía (IEO-CSIC), Servicios Centrales de Madrid, 28080 Madrid, Spain

M. Catalán
Real Instituto Y Observatorio de La Armada, 11110 San Fernando, Cádiz, Spain

R. Casillas · M. C. Martín-Luis
Departamento de Biología Animal, Edafología Y Geología, Universidad de La Laguna, Tenerife, Spain

P. J. González (ed.), *El Hierro Island*, Active Volcanoes of the World,
https://doi.org/10.1007/978-3-031-35135-8_4

Abstract

Active volcanoes are key laboratories to carry out detailed research -and monitoring- about the history of magmas before, during and after eruptions. Tagoro, the submarine active volcano at El Hierro Island (Canary archipelago), is a highly favorable case to assess and monitor its daily ongoing behaviour, as well as to study the links between the processes of magma genesis occurring at depth and their derived eruptive events at the surface. In this interdisciplinary research we combine new results of classical petrology (petrography, geochemistry, and thermodynamics) on the volcanic products expelled by Tagoro during the 2011–2012 eruption, with a high-resolution (5 m grid) bathymetry model carried out during 2017, and recent data from magnetometry, to refine the current knowledge of this eruption. Our results mainly reveal (i) slight magma differentiation and mixing processes at c. 12 km depth during a continuous eruptive pulse; (ii) a similar magmatic evolution and residence times at depth between previous and 2011–2012 eruptions on the island; (iii) an insignificant interaction of external fluids with the magma at depth or within the ascent conduit; (iv) a present-day magnetometric anomaly under the Tagoro's area; (v) a minimum volume estimate for the magma withdrawn from the plumbing system at depth.

Keywords

Magmatic systems · Ocean Island volcanoes · Petrology · Geobarometry · El Hierro

4.1 Introduction

The scientific interest to advance our knowledge of how magma reservoirs behave and evolve is a fundamental and long-lasting target in Earth Sciences in general and in volcanology-petrology-geochemistry in particular, as it is directly related to the type of hazards that volcanoes may generate. When an eruption is already inevitable, the magmatic evolution under the volcano strongly depends on how the plumbing system behaves at depth. Yet, direct access to this information in nature is challenging and infrequent. Hence, combining exhaustive petrological studies of erupted products with volcano monitoring data recorded prior to and during an eruption becomes extremely useful to achieve such purpose (e.g. Scandone and Malone 1985; Saunders et al. 2012; Martí et al. 2013a,b; Tárraga et al. 2014; Albert et al. 2016, 2019). Tagoro submarine volcano, formed 1.8 km away from the southern coast of the El Hierro Island (Canary archipelago) during the 2011–2012 eruption, is an exceptional natural laboratory of an active volcanic system that allows us to study the magmatic conditions that led to eruption with direct implications to forecast the possible occurrence of the next eruption. In fact, in a recent work at Tagoro, it has been demonstrated that once the magma source is triggered at depth, the geochemical signal (of helium isotopic ratios) in an already erupting system, can be received well in advance of the geophysical signals (Álvarez-Valero et al. 2018). This has also been observed in e.g. Etna volcano (Paonita et al. 2016, 2021).

In addition to the considerably increasing scientific interest on El Hierro, the 2011–2012 eruption and the consequent formation of Tagoro volcano has provided a unique opportunity to combine monitoring and petrological data to infer how an intraplate oceanic system prepared for a new eruptive episode (e.g. Stroncik et al. 2009; López et al. 2012; Fraile-Nuez et al. 2012; Carracedo et al. 2012; Pérez-Torrado et al. 2012; Padrón et al. 2013; Santana-Casiano et al. 2013, 2016; Martí et al. 2013a,b; Domínguez et al. 2014; Longpré et al. 2014, 2017; Álvarez-Valero et al. 2018; Taracsák et al. 2019). However, despite this intense research, there are essential aspects of the pre-, syn-, and post-eruption behaviour of the magmatic system that still remain elusive, such as (i) assessing the evolution of the El Hierro subvolcanic system since its

previous status before the 2011–2012 submarine eruption to the present day, as well as (ii) estimating the minimum volume of magma available in the deep reservoir(s). This interdisciplinary study combines results of petrology (petrography, mineral chemistry and thermodynamic modelling), geochemistry (bulk rock composition and stable isotopes), and geophysics (high-resolution bathymetry and magnetometry) with the aim of contributing to these questions.

4.2 Overview of Tagoro and El Hierro's Geology

El Hierro is the most occidental (27°5′–27°37′ N; 18°14′–18°16′W) of the volcanic islands of the Canary archipelago in the Atlantic Ocean. All the islands in the Canary archipelago except La Gomera, record volcanic activity during the Holocene (Martí et al. 2013a). According to historic records, in the last 600 years there have been more than ten volcanic eruptions in Lanzarote (1730–1736, 1824), Tenerife (1704, 1705, 1706, 1798, 1909) and La Palma islands (1585, 1646, 1677, 1712, 1949, 1971) (Romero 1991). Typically, the eruptions were characterised by a short period of activity (from few weeks to months), and classified as Hawaiian and Strombolian types building cones with different sizes and lava flow volumes (e.g. Romero 1991; Dóniz et al. 2008). Phonolitic volcanism is also present on the archipelago, although subordinated to mafic volcanism (Pellicer 1975, 1977; Fuster 1993; Balcells and Gomez 1997a, 1997b; Carracedo et al. 2001; Pedrazzi et al. 2014).

El Hierro, with a surface of 280 km^2, has been traditionally assumed to be the youngest island of the archipelago, as the oldest dated subaerial rock comes from 1.12 Ma, but the volcanic edifice is also composed of a 4000 m submarine succession of unknown age (Guillou et al. 1996). Its base displays a circular shape, yet from an aerial view it is more similar to a tetrahedron due to the occurrence of three large volcanic-derived landslides (NW, NE and S) (Carracedo 2011). Becerril et al. (2015, 2016) state that the volcano-structural evolution of the island was controlled by a predominant NE–SW strike, which coincides with the main regional trend of the Canary archipelago as whole, and two other dominant structural directions (N–S and WNW–ESE).

The island registered four main eruptive events that formed and shaped the current morphology of the island, at 1.1 Ma; 600–176; 176–134; and 21–2.5 ka (Carracedo et al. 2001).

In October 2011, after three months of volcanic unrest characterised by more than 10,000 earthquakes (magnitude up to 4.3), 5 cm of ground deformation, and significant changes in gas emissions at El Hierro Island, an underwater eruption gave rise to a new shallow submarine volcano (Tagoro) c. 1.8 km southward of La Restinga village at the south of the island (Fig. 4.1). The eruption released large quantities of mantle-derived gases, solutes and heat into the surrounding waters, CO_2 and He fluxes intensified few days before the seismic events and eruption (Padrón et al. 2013; Melián et al. 2014). Periodic bathymetric mapping carried out by the Spanish Institute of Oceanography (IEO) located the main vent and indicated a major growth of the volcano from an initial 300 m depth to 88 m below the sea surface (Fig. 4.1; e.g. Fraile-Nuez et al. 2012, 2016, 2022, Chap. 8 in this book).

The stratigraphic, petrological and geochemical data obtained from this eruption suggest that Tagoro is a submarine monogenetic volcano developed on the offshore slope of El Hierro Island, characterized by the eruption of mafic alkaline magmas, mainly basanites (e.g. Martí et al. 2013a, b; Longprè et al. 2014; Álvarez-Valero et al. 2018). Recent detailed studies of the petrologic and geochemical features of other offshore products previous to Tagoro (Stroncik et al. 2009), as well as for the 2011–2012 event (e.g. Martí et al. 2013a,b; Longprè et al. 2014) described its plumbing system at depth, suggesting a combination of magma mixing events with subsequent fractionation at uppermost mantle depths.

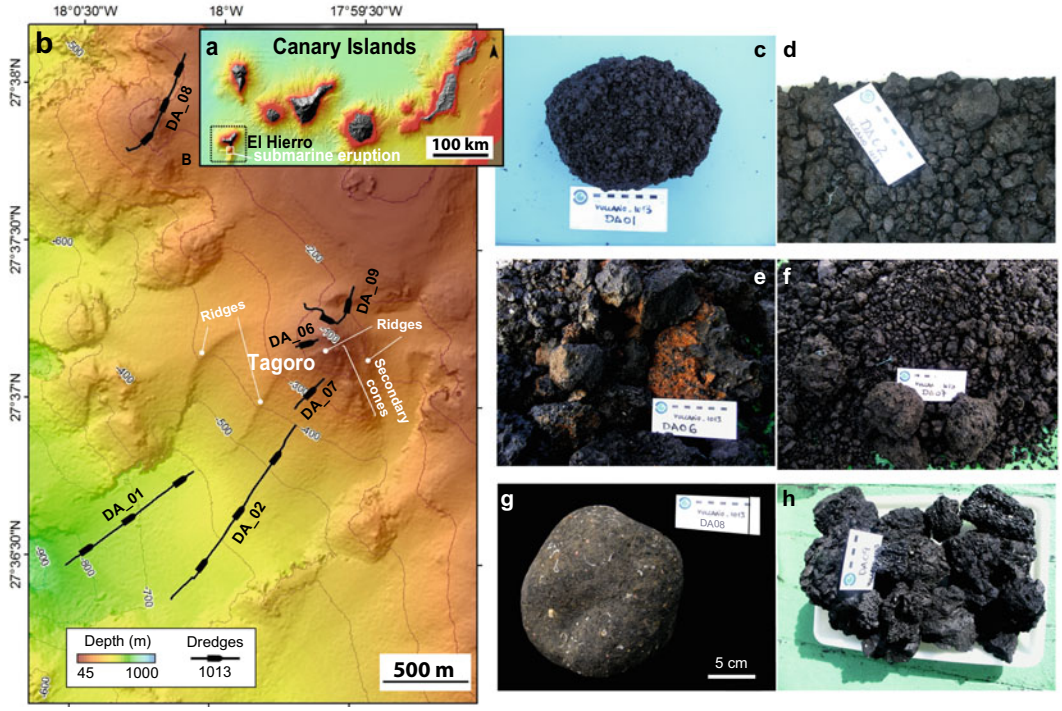

Fig. 4.1 **a** Location of the submarine eruption and El Hierro Island within the Canary archipelago; **b** Bathymetric map of Tagoro volcano area with the location of the rock samples dredged during the VULCANO-1013 oceanographic campaign. Bathymetric data acquired at high resolution of 5 × 5 m during the VULCANA-0417 oceanographic campaign on board of R/V Ramón Margalef (Spanish Institute of Oceanography—IEO); **c**–**h** Hand-specimen examples of some dredged basanites during VULCANO-1013 campaign. Samples DA06 **e**, DA07 **f**, DA09 **h** within the main edifice are from 360 to 110 m b.s.l.; DA01 **c**, DA02 **b** in the lava flow deposits of the SW flank from 850 to 400 m b.s.l., and DA08 **g** from 250 to 170 m b.s.l. 1.8 km northwest of the main edifice

4.3 Methods

To improve our understanding of the magmatic evolution that gave rise to the formation of Tagoro volcano we combined existing data with new geophysical and petrological data. Since 2011 to present, the IEO has carried out systematic oceanographic campaigns of bathymetry (Bimbache, VULCANO and VULCANA projects), as well as sporadic trawl-dredging and magnetometry tasks, to monitor Tagoro's evolution.

The bathymetric data used in this chapter were obtained during the VULCANA-0417 campaign yielding a digital elevation model of Tagoro volcano at 5 m resolution. The dredged samples used in this study were obtained during the VULCANO-1013 oceanographic campaign on board of the Ramón Margalef (IEO) oceanographic vessel from 29 October to 12 November 2013 at different locations on the Tagoro edifice. According to the sea-floor description provided by Somoza et al. (2017), the samples were collected both in the oldest part of the volcanic edifice (Jan–Feb 2012) which is the main exposed one (DA01, DA02, DA06, DA07, DA09), and on the collapsed (and youngest) sector of the edifice (DA08a) formed in October 2011 (Fig. 4.1; Table 4.1). These samples were selected among the entire dredge-load material according to their representativity and freshness (Fig. 4.1c–h). In addition, we studied a pre-2011 eruption sample (DA08m; Álvarez-Valero et al. 2018) to be compared with the 2011–2012 episode.

Table 4.1 Main features summary of the dredges collected at Tagoro

Rock stations	Collecting date	Depth b.s.l. (m)	Eruption area	Hand-specimen description	Techniques
DA01	29-10-2013	792–579	Proximal apron	Angular with prismatic shape composed of alternating levels of coarse sand-fine gravel	EMP, XRF, P–T, D/H, $\delta^{18}O$, NG*
				To fine sand-silt (scoria-lapilli and ash)	
DA02	28-10-2013	643–343	Proximal apron	Well sorted fragmentary material of highly vesiculated vitreous-aphanitic pyroclastics	EMP, XRF, P–T, D/H, $\delta^{18}O$
DA06	28-10-2013	205–196	Main cone	Fragments have red or orange patina of iron oxides and hydroxides that may be due to hydrothermal alterations	
DA07	29-10-2013	358–222	Upper slope	Poorly sorted fragmentary material with angular fragments between 0.5 and 20 cm	EMP, GS
DA08	29-10-2013	269–165	NW outer cone	Massive fragments of lapilli (DA08a); rounded dense bomb rich in olivine crystals (DA8m)	EMP, XRF, D/H, $\delta^{18}O$, NG*, GS
DA09	29-10-2013	225–173	NW main cone	Vesiculated aphanitic and vitreous material (50% vesicles, up to 90%)	EMP

EMPA, electron microprobe analyses; XRF, X-ray fluorescence; P–T, geothermobarometric calculations; NG*, noble gases from Álvarez-Valero et al. 2018; GS, Fe–Mg diffusion geospeedometry in olivine crystals; b.s.l.: below sea level.

Whole-rock major and trace element concentrations were determined by X-ray fluorescence (XRF) analysis with a Rigaku RIX2000 spectrometer at Yamagata University (Japan). Operating conditions were 50 kV accelerating voltage and 50 mA current. The preparation method of the glass disks and the calibration methods for major and trace elements based on Yamada et al. (1995). The standards used in the analyses are the GSJ (Geological Survey of Japan) igneous rocks series. Analytical uncertainties are 5% for Nb, Zr, Y, Sr, Rb and Ni, 10% for V and Cr, and 5–15% for Ba. The range of uncertainties for a single element is based on the concentration range observed in standards.

Major element contents in glass and minerals were analysed on thin sections using a JEOL JXA-8230 electron microprobe at the Scientific and Technological Centre of Barcelona University (CCiTUB). Operating conditions were 20 kV acceleration voltage, 15 nA beam current, 2 μm beam diameter (using a defocused beam of up to 20 μm to minimise sodium mobility) and counting time of 10 s per element. The estimated accuracy and standards used were: SiO_2 (±0.13%, wollastonite); Al_2O_3 (±0.09%, corundum); TiO_2 (±0.13%, rutile); Cr_2O_3 (±0.14%, Cr_2O_3); Na_2O (±0.68%, albite); MgO (±0.11%, periclase); MnO (±0.16%, rhodonite); FeO (±0.11%, Fe_2O_3); ZnO (±0.11%, sphalerite); K_2O (±0.19%, feldspar); and CaO (±0.02%, calcium standard) and VO_3 (±0.20%, vanadium metal).

Crystallographic orientations of the compositional profiles were estimated through SHAPE sofware (Dowty 1987) by matching the BSE images with the 2D section view. Crystal DA07 was modelled employing a forsterite model based on Roubault et al. (1963) (Miller Indexes: [010], [001], [021], [110] with central distances 1, 2, 1.4, 1.05, respectively). Whereas, for crystal DA08m we applied 1.8 for the central distance of [001] and 0.4 for the section height.

For the stable isotope analysis of bulk-rock we cut and discarded several centimeters of material from the surface to avoid any potential late isotopic modification by weathering. The hydrogen and oxygen isotopic analyses were carried out at the Servicio General de Análisis de Isótopos Estables (NUCLEUS—University of

Salamanca, Spain). Oxygen in glass and phenocrysts was extracted by fluorination (Clayton and Mayeda 1963) employing a Synrad 25W CO_2 laser (Sharp 1990) and ClF_3 as reagent (e.g. Borthwick and Harmon 1982), and oxygen isotope ratios were measured on a VG-Isotech SIRA-II dual-inlet mass spectrometer. Both internal and international reference standards (NBS-28, NBS-30) were run to check accuracy and precision. Long-term reproducibility for repeated determination of reference samples was better than ± 0.2% (1σ). Results are reported in $\delta^{18}O$ notation relative to the Vienna Standard Mean Ocean Water (V-SMOW) standard, using a $\delta^{18}O$ value of 9.6% for NBS-28 (quartz) for the mass spectrometer calibration.

D/H ratios were determined on another SIRA-II mass spectrometer on H_2 gas obtained by reduction over hot depleted-U of the water released by induction heating of samples. A vacuum line (Bigeleisen et al. 1952), following the procedures described by Godfrey (1962) with modifications (Jenkin 1988), was used for gas extraction. Samples were loaded into degassed platinum crucibles that were placed in quartz reaction tubes and heated under vacuum to 125° C overnight to remove any adsorbed H_2O. Results are reported in δD notation relative to the V-SMOW standard, using a δD = − 66.7% for NBS-30 (biotite) for the mass spectrometer calibration. Long-term reproducibility for repeated determination of reference samples was better than ± 2% (1σ). The amount of H_2 recovery is known by a baratron gauge reading, which measures the total hydrogen (non-condensables) derived from water according to the ideal gas law. Then, we calculated the water content (% H_2O), as a function of the amount of H_2 obtained and the sample weight (wt%).

For the magnetometric measurements, we employed a Marine Seaspy magnetometer. This equipment was placed 200 m astern of the ship to guarantee an accuracy of more than 1 nT. The rate of acquisition of the data was 0.166 Hz, which would imply a spatial resolution along the line of 31 m at a speed of 10 knots (i.e. 18.52 km/h). The position of the vessel was obtained from ship's own computer system. These locations were affected by a correction that correctly positioned the measurement.

We used Güimar (Tenerife Island) geomagnetic observatory data to extract the contribution by external fields. The internal field contribution was extracted using the IGRF-12 model (Thébault et al. 2015). To determine the depth to the top of magnetic basement of magnetic bodies we have used two different approaches. First, we have applied Werner Deconvolution (Hartman et al. 1971; Ku and Sharp 1983). It is a powerful tool for the interpretation of magnetic profiles. To get a set of depth solutions using this method we have to define the size of a window. The mathematical procedure started using the smallest window size selected. The window moves along the profile to the end. Then the window size is incremented and the entire profile is processed again until the maximum size is reached. As minimum and maximum size we set 100 and 3000 m respectively, and the window expansion and shift increments were set at 100 and 500 m respectively. We have obtained a set of solutions that show a homogenous picture. Most of solutions fall between 700 m and 2 km below the sea level (b.s.l.). To cross-check this, we have obtained the radial average spectrum of the magnetic anomaly map showing a reliable solution. Spector and Grant (1970) stated that the shape of the power-density spectrum of the magnetic anomaly is strongly controlled by the average depth of the magnetic causative body. Specifically, the spectrum decays exponentially with wavenumber, at a rate of decay proportional to the average depth to the top of the magnetic source.

4.4 Results

4.4.1 Bathymetry and Dredged Samples Description

Two large morphological units can be distinguished in the volcanic materials erupted by the 2011–2012 eruption (Fig. 4.1b), namely, the first one that built the main edifice and the second one constituting the flow of material that mainly

extends to the southwest (Vázquez et al. 2022, Chap. 7 in this book). The main edifice is at 88 m b.s.l., with slopes dipping 20°–34°, extending up to a depth of c. 400 m b.s.l., where the slope decreases below 20°. The base of this edifice is pseudo-circular with diameter ranging from 0.9 to 1.2 km, and irregularities in shape due to the presence of two sets of morphological elements: (i) four ridges, two of them with a NE–SW direction located on the west flank of the main edifice, a third with an ENE–WSW trend that crosses the proximal secondary cone, and another one with a NNW–SSE orientation located on the eastern flank of the main edifice (Vázquez et al. 2016); (ii) several secondary cones from NNW to SSE decreasing in height (from 88 to 247 m b.s.l.; Fig. 4.1b) and size, showing at least 13 old vents (see also Vázquez et al. 2016).

In hand-specimen, the dredged materials show in general the typical features of basaltic products of a submarine explosive eruption (Fig. 4.1c–h). Samples in dredge DA01 are fragmentary to a large extent. These fragments range from (i) very vesiculated vitreous-aphanitic material with vesicles and quenched glass oriented in parallel and incipient radial disjunction similar to pillow-lava fragments or the so-called "pieces of cake" (sample DA01b), coming from the pillow-lava flow; to (ii) fragments of consolidated lapilli (sample DA01a), likely related to a previous collapsed pyroclastic deposit of the first edifice. In dredge DA02, the samples are fragments of lava flows, vitreous-aphanitic with vesicle contents becoming progressively higher towards the centre of each fragment, coming from the lava sliding of the last edifice. Materials in dredges DA03 and DA04 are glassy, highly vesiculated pyroclastic fragments (c. 70 and 50% vesicles, respectively). The former are similar to the amphora-like floating lava balloons described by Somoza et al. (2017). Sample DA06 is a heterogeneous fragmentary material of mostly vitreous-aphanitic fragments, with a variable range of vesicle amounts and sizes, and most probably represents pyroclastic material of lapilli and ash after a more highly explosive phase of activity. Sample DA07 consists of fairly homogeneous pyroclastic fragments mixed with lava fragments of various different morphologies. Samples in dredge DA08 are heterogeneous with fragments of lapilli (DA08a), and a rounded basanite bomb (DA08m) with numerous colonies of black corals and other organisms. Samples in dredge DA09 are pyroclastic fragments (scoria and lapilli) from explosive eruptions during the last edifice building episode. The studied sample from dredge DA09 is highly vesiculated (50–90%).

4.4.2 Petrographic Analysis

The bubble-rich hypidiomorphic basanites erupted in 2011–2012 generally contain (micro)phenocrysts of mainly olivine from subhedral to anhedral, clinopyroxene (augite), ulvospinel (titanomagnetite), and locally plagioclase (mostly as microlites within the mesostasis). Olivine phenocrysts are generally characterized by reverse forsterite (Fo) zoning patterns from core to rim followed by a Fo decrease towards the edge. Groundmass textures range from hypocrystalline, aphanitic, microcrystalline to porphyric with a wide range of bubble volumes and shapes (Fig. 4.2; see also Martí et al. 2013a, b). Sample DA08m shows the highest modal proportion of phenocrysts, as well as two generations of phenocrysts with local undulated olivine and pyroxene, while samples DA07, DA02 and DA01b display the higher volumetric proportion of vesicles. DA01a and DA08a are more massive than the latter, thus showing a lower vesicular volume. DA01a also shows local undulated olivine phenocrysts (Fig. 4.2). According to the representative hand-specimen and petrographic features of all the collected samples, we selected (i) DA01b, DA02, DA07, DA08a, DA08m, DA09 for the mineral chemistry study in order to analytically cover all the crystals' variability. We also focused on the glasses aiming to track any potential variation compared to their respective bulk rock, thus assessing the compositional evolution of the residual melts; and (ii) samples DA01a, DA01b, DA02, DA08a, DA08m covering the whole range of macroscopic features of all the dredged samples, for the analysis of bulk composition.

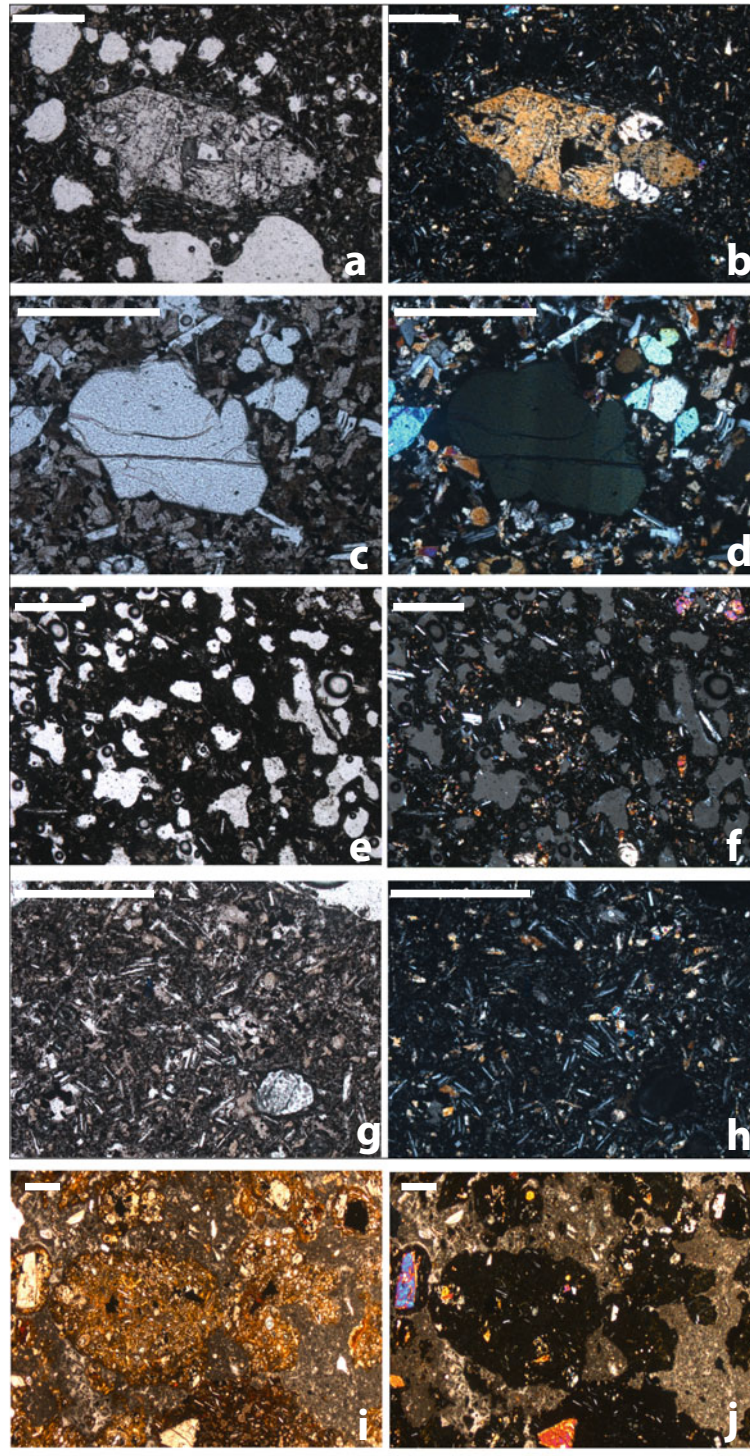

Fig. 4.2 Photomicrographs of the studied samples under plane-polarized light (left column) and cross-polarized light (right column) highlighting: **a**, **b** euhedral olivine phenocryst with uniform optical extinction (DA01b) within a glassy and bubbly groundmass; **c**, **d** subeuhedral olivine phenocryst with undulatory extinction (DA08m) within a microcrystalline groundmass. Similar olivines are also locally observed in DA01a. **e**, **f** Sample DA07 with mostly glassy groundmass and abundant vesicles. **g**, **h** Massive DA01a poor in vesicles and rich in (micro) phenocrystals of Ol, Pl, Cpx and secondary oxides. **i**, **j** Different glass microdomains in sample DA08a. In each image the scale bar is 500 microns

4.4.3 Whole-Rock Geochemistry (X-Ray Fluorescence, XRF)

With the exception of sample DA08m, all samples i.e. DA01a, DA01b, DA02, DA08a are compositionally very similar (Table 4.2; Figs. 4.3, 4.4). All samples are alkaline basanites with MgO and SiO_2 contents of 7.18–8.11 wt% and 42.45–42.94 wt%, respectively, whereas sample DA08m contains 12.56 wt% MgO and 41.24 wt% SiO_2. Sample DA08m also displays different abundances of some trace elements such as Cr (467 ppm) and Ni (299 ppm), with respect to the rest of samples that contain 147–225 ppm Cr, and 94–139 ppm Ni.

4.4.4 Glass and Mineral Chemistry (Electron Microprobe)

Glasses are characterized by a constant composition for each particular eruptive period, yet different compositional ranges as a function of their eruption chronology (along the five months event) and their location at the surface. Only samples belonging to the first edifice (i.e. DA01a and DA08a from the first eruption period starting in October 2011) have more evolved compositions (> 50% SiO_2 wt%) phono-tephrite and phonolite, respect to the subsequently erupted samples that formed the last edifice (ca. 45–48 SiO_2 wt%) (Figs. 4.3, 4.4; Table 4.2). The latter are also compositionally very similar to the glasses of the pre-2011 eruption (i.e. sample DA08m) (45–46 SiO_2 wt%).

Olivine phenocrysts have display a slight reverse zoning patterns and do not vary systematically with their host whole-rock composition. Only the pre-2011 sample DA08m, shows a lower Fo content (Fo_{78}, Fig. 4.2; Table 4.2). Clinopyroxene phenocrysts (classified as diopside) are also similar in composition for all samples with average values of 7 FeO wt%, 22 CaO wt% and 13 MgO wt%. Plagioclase (bytownites) show a fairly constant composition for all samples of c. $An_{78\text{-}86}$. Local oxide minerals are also present as secondary phases (Fig. 4.2).

4.4.5 Geothermobarometry

Pressure (P) and temperature (T) estimates were constrained by applying and combining classical geothermobarometers and thermodynamical modelling through the thermodynamic database of rhyolite-MELTS software v.1.2.0 (Ghiorso and Sack 1995; Asimow and Ghiorso 1998). Concerning the former (e.g. Albarede 1992; Nimis 1999; Putirka 2005, 2008), we applied them between pairs of minerals (rim versus rim) or mineral-glass at equilibrium, i.e. when the equilibrium constant ($K_D = X_{FeO}/X_{MgO}$) mineral (X_{FeO}/X_{MgO}) melt were ca. 0.3 for olivine and clinopyroxene versus glass (e.g. Roeder and Emslie 1970; Putirka et al. 1996; Stroncik et al. 2009). Pressure results of 1.2–2.3 GPa are however locally not in line with the depths from previous studies (e.g. Stroncik et al. 2009; Martí et al. 2013a,b; Longprè et al. 2014). Hence, we are cautious because this inconsistency is related to the differences between the input parameters used in the mentioned experiments and the real conditions of the Tagoro sub-volcanic system: for instance, orthopyroxene is normally assumed in the equilibrium system of the experiments (e.g. Putirka 2008), yet it is absent in the Tagoro samples; or the silica activity experiments carried out under conditions of peridotites (e.g. Albarede 1992) but not properly basanites as the Tagoro rocks. Regarding the thermodynamical modelling, it allows to constrain P and T by considering equilibrium among the phases involved in the main paragenesis, as well as the observed versus computed modal proportions of glass and crystals within the groundmass. For the modelling calculations we used the whole-rock compositions (Table 4.2a) as input "parental" magmas into the rhyolite-MELTS software and retrieved phenocrystic assemblages and abundances with chemical compositions for various T–P–H_2O conditions (an initial 1–1. 5 wt% H_2O) under oxygen fugacity (fO_2) conditions of 1 log units above the Niquel-Niquel-Oxide (NNO) buffer (Ban et al. 2008) at pressures from 0.1 to 0.5 GPa until equilibria were achieved; i.e. we finally compared the best fit of SiO_2–X_{Mg}–T–P conditions between the calculated and the

Table 4.2 Geochemical results of the studied samples

(a)

	SiO_2	Al_2O_3	TiO_2	FeO	Fe_2O_3	MgO	MnO	CaO	Na_2O	K_2O	P_2O_5
D1a	42.94	13.45	4.74	11.24	2.21	7.18	0.18	10.72	3.65	1.49	0.89
D1b	42.57	12.82	4.75	11.3	2.22	8.07	0.18	10.95	3.57	1.44	0.81
D2	42.45	12.78	4.76	11.24	2.2	8.11	0.17	10.93	3.66	1.43	0.81
D8a	42.79	13.34	4.68	11.34	2.22	7.29	0.18	10.62	3.71	1.51	0.89
Pre-2011 eruption											
D8m	41.24	10.74	4.13	11.69	2.29	12.56	0.18	11.32	2.85	1.04	0.87

(a)

	Rb	Ba	Sr	Zr	Y	Nb	Cr	Ni	V	Zn	Cu
D1a	33	359	975	402	35.5	78.4	151	94.3	333	131	75.5
D1b	31.5	337	906	365	32.9	70.9	225	138	343	126	97.1
D2	30.3	334	905	365	32.7	70.4	224	139	335	125	88.4
D8a	33.8	366	979	406	36.1	78.7	147	96.4	321	134	74
Pre-2011 eruption											
D8m	19.8	285	823	287	28.5	58.3	467	299	323	118	89.8

(b)

	SiO_2	Al_2O_3	TiO_2	FeO	MgO	MnO	CaO	Na_2O	K_2O	Total
DA01b	48.47	15.51	2.92	10.04	2.27	0.28	5.67	5.69	3.41	94.26
DA01b	47.97	16.08	3.09	9.78	2.40	0.21	5.93	6.61	3.24	95.33
DA01b	48.26	16.90	2.99	10.24	1.77	0.24	4.38	6.34	3.87	94.99
DA01b	46.79	16.04	3.55	11.20	2.62	0.30	5.91	7.10	3.51	97.05
DA01b	46.56	16.12	3.43	10.43	2.78	0.19	6.83	7.02	3.49	96.88
DA01b	46.77	15.98	3.58	10.76	2.51	0.26	6.30	7.23	3.38	96.81
DA01b	46.62	16.21	3.39	10.14	2.79	0.23	6.77	6.65	3.34	96.15
DA01b	47.18	16.51	3.33	10.15	2.76	0.19	6.79	6.70	3.24	96.87
DA01b	47.79	16.50	3.06	10.36	2.71	0.20	6.17	6.71	3.58	97.13
DA01b	49.83	16.87	2.65	8.49	2.37	0.21	5.85	5.48	3.45	95.21
DA02	46.08	14.91	4.51	12.19	3.65	0.30	8.67	4.04	2.83	97.24
DA02	46.29	15.41	4.55	12.21	3.31	0.25	7.55	4.67	2.96	97.27
DA02	45.41	15.04	4.62	11.99	3.40	0.23	8.38	4.53	2.81	96.46
DA08a	52.90	19.63	1.00	5.51	0.45	0.04	0.10	7.36	6.82	93.84
DA08a	54.41	21.64	0.87	5.17	0.54	0.09	0.34	10.59	5.56	99.21
DA08a	52.15	20.86	0.54	5.09	0.61	0.10	1.94	9.49	6.55	97.37
DA08a	51.83	20.66	0.68	6.34	0.95	0.17	0.70	9.87	7.11	98.32
DA08a	51.24	21.02	0.61	5.95	0.94	0.16	1.03	9.39	6.69	97.03
DA08a	52.56	20.62	0.58	5.88	0.77	0.11	0.70	9.82	7.21	98.26
DA08a	53.36	21.35	0.94	5.54	0.73	0.11	0.21	9.72	7.21	99.20
DA08a	50.91	20.09	0.66	4.78	0.41	0.09	1.50	8.46	6.62	93.53
DA08a	51.23	19.68	0.64	5.66	0.54	0.11	0.05	8.13	7.10	93.14
DA09	44.81	14.96	4.71	11.50	3.86	0.22	9.35	4.99	2.19	96.64

(continued)

Table 4.2 (continued)

(b)

	SiO_2	Al_2O_3	TiO_2	FeO	MgO	MnO	CaO	Na_2O	K_2O	Total
Pre-2011 eruption										
DA08m	45.40	15.13	4.15	10.96	4.44	0.20	8.85	4.77	2.43	96.43
DA08m	45.05	15.82	4.38	11.01	4.54	0.26	8.86	4.95	2.20	97.09
DA08m	45.57	15.77	4.34	10.60	4.48	0.22	8.73	4.78	2.25	96.81
DA08m	45.64	15.76	4.33	10.71	4.58	0.26	8.78	4.68	2.31	97.11
DA08m	45.56	15.70	4.25	10.68	4.48	0.19	8.93	4.77	2.25	96.86
DA08m	45.83	15.62	4.26	10.75	4.70	0.16	8.92	4.78	2.27	97.37
DA08m	46.45	15.83	4.31	10.59	4.31	0.18	8.83	4.96	2.35	97.85
DA08m	45.35	15.61	4.37	10.77	4.53	0.21	8.84	4.94	2.14	96.81
DA08m	45.78	15.79	4.34	10.81	4.61	0.23	8.72	4.96	2.34	97.67
DA08m	45.28	15.51	4.30	10.84	4.42	0.16	8.79	4.93	2.21	96.47
DA08m	45.75	15.61	4.29	10.75	4.27	0.16	8.91	5.02	2.25	97.09

(c)

	SiO_2	Al_2O_3	TiO_2	FeO	MgO	MnO	CaO	Na_2O	K_2O	Total
DA01b	40.03	0.02	0.03	17.42	41.79	0.24	0.27	0.02	0.01	99.87
DA01b	40.40	0.00	0.03	16.71	42.46	0.25	0.26	0.04	0.00	100.17
DA01b	40.04	0.02	0.04	16.98	42.41	0.23	0.26	0.00	0.01	100.00
DA01b	40.09	0.02	0.01	17.61	42.18	0.24	0.28	0.03	0.01	100.51
DA01b	40.76	0.00	0.03	15.29	43.75	0.21	0.27	0.00	0.01	100.34
DA01b	40.55	0.04	0.03	15.23	43.89	0.21	0.27	0.00	0.01	100.27
DA01b	40.87	0.04	0.05	14.20	44.46	0.21	0.24	0.02	0.00	100.16
DA01b	41.01	0.01	0.02	16.80	42.97	0.20	0.19	0.02	0.00	101.24
DA01b	40.94	0.03	0.03	17.21	41.92	0.26	0.29	0.00	0.01	100.71
DA01b	40.01	0.02	0.05	17.73	41.92	0.24	0.23	0.03	0.00	100.22
DA01b	40.53	0.04	0.03	16.45	42.33	0.22	0.28	0.02	0.01	99.95
DA01b	40.30	0.04	0.03	16.42	42.98	0.26	0.28	0.03	0.00	100.40
DA01b	40.23	0.00	0.05	17.73	42.21	0.23	0.26	0.00	0.00	100.73
DA01b	40.21	0.05	0.02	17.21	42.25	0.28	0.26	0.00	0.01	100.29
DA01b	40.29	0.06	0.03	17.55	41.47	0.21	0.28	0.00	0.00	99.90
DA01b	41.36	0.03	0.04	17.36	41.68	0.25	0.29	0.03	0.01	101.09
DA01b	40.47	0.03	0.03	16.92	42.09	0.24	0.29	0.06	0.02	100.18
DA02	39.82	0.03	0.03	16.59	43.35	0.23	0.27	0.00	0.01	100.38
DA02	40.47	0.04	0.03	17.31	42.16	0.26	0.28	0.04	0.00	100.60
DA02	40.47	0.04	0.04	15.93	43.09	0.23	0.24	0.02	0.00	100.09
DA02	40.33	0.05	0.02	16.15	42.81	0.24	0.24	0.00	0.00	99.86
DA02	40.51	0.02	0.04	17.34	41.80	0.21	0.27	0.01	0.01	100.22
DA02	40.63	0.00	0.04	17.10	42.79	0.26	0.29	0.00	0.02	101.14
DA02	40.68	0.05	0.04	17.87	41.59	0.26	0.32	0.00	0.03	100.84
DA02	40.19	0.04	0.02	17.20	42.45	0.26	0.26	0.01	0.00	100.45

(continued)

Table 4.2 (continued)

(c)

	SiO_2	Al_2O_3	TiO_2	FeO	MgO	MnO	CaO	Na_2O	K_2O	Total
DA02	40.97	0.06	0.03	15.79	43.15	0.22	0.28	0.00	0.01	100.53
DA02	40.19	0.01	0.02	15.52	43.60	0.19	0.28	0.00	0.01	99.87
DA02	40.39	0.04	0.01	16.85	42.58	0.25	0.26	0.04	0.01	100.48
DA02	40.30	0.02	0.03	16.69	43.02	0.22	0.27	0.02	0.02	100.67
DA02	40.59	0.04	0.07	17.31	41.54	0.25	0.28	0.00	0.03	100.15
DA02	40.29	0.05	0.09	18.29	41.61	0.24	0.32	0.01	0.01	100.93
DA07	40.37	0.06	0.04	17.19	42.80	0.25	0.18	0.00	0.00	100.91
DA07	40.68	0.05	0.02	14.47	44.92	0.21	0.20	0.01	0.02	100.63
DA07	40.43	0.01	0.04	17.39	42.43	0.28	0.27	0.00	0.01	100.91
DA07	40.35	0.07	0.06	17.60	42.70	0.25	0.26	0.03	0.01	101.36
DA07	40.25	0.05	0.04	17.24	42.71	0.24	0.27	0.00	0.01	100.83
DA07	40.26	0.03	0.06	18.79	40.92	0.26	0.35	0.01	0.00	100.71
DA08a	39.99	0.04	0.02	19.64	40.80	0.27	0.22	0.00	0.02	101.02
DA08a	39.78	0.00	0.03	19.61	41.36	0.28	0.22	0.00	0.04	101.33
DA08a	40.24	0.00	0.07	18.82	41.04	0.29	0.30	0.02	0.01	100.79
DA09	39.81	0.03	0.03	16.38	42.29	0.20	0.25	0.00	0.02	99.04
DA09	40.59	0.07	0.03	14.67	43.93	0.19	0.26	0.00	0.02	99.80
DA09	40.84	0.02	0.02	13.13	44.59	0.17	0.28	0.01	0.00	99.11
DA09	39.93	0.04	0.07	17.65	41.68	0.25	0.27	0.01	0.03	99.94
Pre-2011 eruption										
DA08m	39.85	0.04	0.03	20.08	40.84	0.30	0.21	0.00	0.00	101.36
DA08m	39.12	0.02	0.01	19.71	40.55	0.31	0.20	0.00	0.01	99.94
DA08m	40.22	0.02	0.02	18.30	42.17	0.28	0.13	0.00	0.00	101.15
DA08m	39.89	0.04	0.04	18.83	41.57	0.26	0.14	0.00	0.02	100.82
DA08m	40.38	0.02	0.01	18.08	42.29	0.26	0.11	0.03	0.03	101.23
DA08m	40.37	0.03	0.00	17.31	42.35	0.27	0.18	0.04	0.00	100.56
DA08m	40.73	0.03	0.00	15.42	44.23	0.24	0.29	0.00	0.02	100.98
DA08m	40.11	0.02	0.01	18.91	41.39	0.24	0.13	0.00	0.01	100.81
DA08m	40.60	0.05	0.03	17.35	42.85	0.24	0.16	0.02	0.01	101.35
DA08m	40.54	0.00	0.04	16.12	43.57	0.24	0.33	0.01	0.01	100.88
DA08m	40.26	0.06	0.04	16.16	43.70	0.19	0.32	0.00	0.02	100.81
DA08m	40.60	0.06	0.04	14.88	44.93	0.21	0.23	0.00	0.02	100.98
DA08m	41.11	0.03	0.02	15.56	44.18	0.21	0.27	0.00	0.00	101.40
DA08m	40.52	0.01	0.03	15.49	44.33	0.26	0.23	0.06	0.01	100.95

(d)

	SiO_2	TiO_2	Al_2O_3	FeO	MnO	MgO	CaO	Na_2O
DA01b	47.71	2.12	6.81	8.56	0.22	11.42	21.86	0.79
DA01b	47.33	2.33	7.24	8.34	0.15	11.70	21.79	0.83
DA01b	48.46	2.75	4.44	7.16	0.09	13.56	22.25	0.34

(continued)

Table 4.2 (continued)

(d)

	SiO_2	TiO_2	Al_2O_3	FeO	MnO	MgO	CaO	Na_2O
DA01b	50.40	1.86	4.02	6.01	0.10	14.41	22.23	0.45
DA01b	44.87	4.17	7.97	7.21	0.12	11.73	22.53	0.52
DA01b	48.67	2.90	4.86	7.05	0.11	13.34	22.37	0.45
DA01b	47.84	2.59	6.17	6.44	0.08	13.07	22.35	0.46
DA01b	50.42	1.87	4.14	5.87	0.09	14.16	22.35	0.45
DA01b	46.18	3.22	8.36	6.93	0.14	12.50	21.63	0.60
DA01b	49.79	2.35	4.33	6.82	0.14	14.10	22.18	0.37
DA01b	42.94	4.98	8.85	7.87	0.09	11.01	22.37	0.56
DA01b	48.73	2.95	4.99	6.98	0.12	13.19	22.42	0.44
DA01b	44.34	4.80	8.55	7.85	0.10	11.10	22.29	0.57
DA01b	46.38	3.36	6.96	7.50	0.08	12.23	22.35	0.50
DA01b	48.92	2.25	6.29	6.94	0.13	12.66	21.64	0.63
DA01b	44.98	4.37	7.90	7.60	0.11	11.42	22.35	0.47
DA01b	44.83	4.39	8.26	7.24	0.09	11.39	22.41	0.53
DA01b	49.10	2.81	4.73	7.11	0.13	13.65	22.46	0.42
DA01b	50.34	2.06	3.86	6.50	0.07	14.25	22.25	0.46
DA01b	49.17	2.68	4.87	6.82	0.13	13.43	22.49	0.44
DA02	50.25	2.44	4.21	6.86	0.13	14.04	22.40	0.35
DA02	44.41	4.64	8.49	7.62	0.10	11.31	22.34	0.44
DA02	50.75	2.01	4.15	6.51	0.09	14.26	22.20	0.48
DA02	50.91	1.94	4.09	6.37	0.09	14.22	22.35	0.52
DA02	50.08	2.14	4.13	6.48	0.11	13.93	22.27	0.36
DA02	50.05	2.01	4.10	6.40	0.11	14.10	22.20	0.40
DA07	48.17	2.40	6.25	7.50	0.19	13.04	21.49	0.74
DA07	49.80	2.36	4.41	6.89	0.10	13.93	22.02	0.40
DA07	49.25	2.78	4.60	7.05	0.14	13.50	22.12	0.43
DA07	50.89	1.74	4.10	5.82	0.10	14.33	22.18	0.48
DA07	50.80	1.75	4.14	5.82	0.12	14.35	22.19	0.50
DA07	49.26	2.56	4.28	7.17	0.12	13.90	22.01	0.42
DA08a	47.88	2.50	6.81	7.03	0.12	13.16	21.36	0.83
DA08a	48.78	2.46	4.81	6.75	0.14	14.22	22.23	0.53
DA08a	50.24	2.28	4.15	6.48	0.12	14.02	22.40	0.43
DA08a	48.30	2.47	6.75	6.94	0.12	12.96	21.44	0.71
DA08a	50.26	1.79	4.70	6.92	0.13	13.68	21.56	0.67
DA08a	47.94	2.68	6.67	6.88	0.11	13.04	21.93	0.64
DA08a	49.30	2.34	4.54	6.46	0.13	13.86	22.66	0.50
DA08a	47.26	3.02	6.24	6.90	0.12	12.97	22.35	0.54
DA08a	45.87	3.83	7.55	7.30	0.10	11.90	22.30	0.57

(continued)

Table 4.2 (continued)

(d)

	SiO_2	TiO_2	Al_2O_3	FeO	MnO	MgO	CaO	Na_2O
DA08a	48.11	2.97	5.39	7.32	0.13	13.30	22.03	0.48
DA08a	49.28	2.63	5.04	7.12	0.14	13.81	21.76	0.46
DA08a	48.09	2.49	6.17	7.10	0.13	13.12	22.35	0.66
DA08a	47.01	2.92	7.36	8.09	0.12	11.76	22.15	0.69
DA08a	45.62	4.08	8.34	7.42	0.10	11.91	22.06	0.61
DA08a	45.10	4.34	8.12	7.77	0.12	11.78	21.95	0.58
DA09	49.84	2.13	4.04	6.67	0.13	13.99	21.85	0.42
DA09	49.79	1.96	3.82	6.41	0.11	14.24	22.08	0.35
DA09	42.37	5.38	9.69	8.16	0.09	10.86	22.06	0.58
DA09	49.76	2.14	4.01	6.50	0.11	13.99	22.22	0.40
DA09	44.10	4.55	8.41	7.77	0.13	11.57	21.89	0.56
DA09	49.33	2.24	4.11	6.69	0.11	14.11	22.06	0.44
DA09	44.17	4.76	8.60	7.48	0.09	11.23	22.03	0.51
Pre-2011 eruption								
DA08m	48.30	2.74	5.14	6.87	0.11	13.27	22.59	0.42
DA08m	44.82	4.11	8.36	7.50	0.10	11.31	22.63	0.53
DA08m	48.25	2.87	5.24	7.05	0.14	13.03	22.59	0.53
DA08m	48.31	2.87	5.48	7.04	0.13	12.87	22.66	0.54
DA08m	43.95	4.88	9.15	7.90	0.10	11.11	22.40	0.52
DA08m	48.73	2.82	5.50	7.03	0.15	13.11	22.56	0.42

(d)

	K_2O	Total	Mg/(Mg + Fe_2)	Fe_2/(Fetot)	Al/(Al + Fe_3 + Cr)	Jadeite	Acmite	Diopside
DA01b	0.01	99.56	0.753	0.779	0.835	0.048	0.009	0.943
DA01b	0.00	99.76	0.779	0.711	0.809	0.048	0.011	0.940
DA01b	0.02	99.13	0.800	0.844	0.848	0.021	0.004	0.976
DA01b	0.00	99.75	0.822	0.924	0.926	0.030	0.002	0.967
DA01b	0.02	99.24	0.806	0.696	0.837	0.032	0.006	0.962
DA01b	0.01	99.86	0.795	0.868	0.880	0.029	0.004	0.967
DA01b	0.01	99.45	0.813	0.830	0.888	0.030	0.004	0.966
DA01b	0.02	99.71	0.812	0.997	0.997	0.032	0.000	0.968
DA01b	0.00	99.70	0.811	0.751	0.872	0.038	0.006	0.957
DA01b	0.01	100.16	0.802	0.912	0.911	0.024	0.002	0.974
DA01b	0.01	98.78	0.804	0.610	0.802	0.033	0.008	0.959
DA01b	0.00	99.86	0.784	0.930	0.935	0.030	0.002	0.968
DA01b	0.00	99.71	0.759	0.798	0.884	0.036	0.005	0.959
DA01b	0.01	99.48	0.796	0.745	0.837	0.031	0.006	0.963
DA01b	0.03	99.56	0.762	1.018	1.014	0.046	-0.001	0.954
DA01b	0.00	99.30	0.760	0.845	0.904	0.031	0.003	0.966

(continued)

Table 4.2 (continued)

(d)

	K_2O	Total	Mg/(Mg + Fe_2)	Fe_2/(Fetot)	Al/(Al + Fe_3 + Cr)	Jadeite	Acmite	Diopside
DA01b	0.00	99.25	0.772	0.828	0.904	0.035	0.004	0.962
DA01b	0.01	100.45	0.802	0.844	0.858	0.026	0.004	0.970
DA01b	0.01	99.94	0.812	0.907	0.900	0.030	0.003	0.967
DA01b	0.02	100.11	0.794	0.912	0.920	0.029	0.003	0.968
DA02	0.03	100.80	0.789	0.978	0.975	0.025	0.001	0.975
DA02	0.00	99.45	0.760	0.835	0.905	0.029	0.003	0.968
DA02	0.03	100.61	0.803	0.959	0.956	0.032	0.001	0.966
DA02	0.02	100.62	0.807	0.952	0.949	0.035	0.002	0.963
DA02	0.03	99.63	0.791	1.012	1.013	0.027	0.000	0.974
DA02	0.02	99.52	0.806	0.945	0.942	0.027	0.002	0.971
DA07	0.01	99.85	0.814	0.709	0.801	0.043	0.011	0.946
DA07	0.00	99.98	0.788	0.968	0.965	0.028	0.001	0.971
DA07	0.00	99.95	0.779	0.969	0.968	0.030	0.001	0.969
DA07	0.02	100.04	0.808	1.041	1.043	0.036	-0.001	0.965
DA07	0.01	100.00	0.814	1.004	1.004	0.036	0.000	0.964
DA07	0.01	99.79	0.801	0.856	0.854	0.026	0.004	0.970
DA08a	0.00	99.83	0.833	0.669	0.805	0.048	0.012	0.940
DA08a	0.03	100.00	0.863	0.597	0.714	0.027	0.011	0.962
DA08a	0.01	100.19	0.799	0.972	0.970	0.030	0.001	0.969
DA08a	0.00	99.86	0.795	0.860	0.907	0.047	0.005	0.949
DA08a	0.00	99.76	0.790	0.936	0.938	0.045	0.003	0.952
DA08a	0.02	100.01	0.815	0.765	0.853	0.039	0.007	0.954
DA08a	0.00	99.87	0.835	0.753	0.801	0.029	0.007	0.964
DA08a	0.01	99.51	0.828	0.694	0.807	0.032	0.008	0.961
DA08a	0.02	99.52	0.787	0.786	0.872	0.036	0.005	0.959
DA08a	0.00	99.79	0.800	0.808	0.844	0.029	0.005	0.965
DA08a	0.00	100.31	0.791	0.914	0.921	0.030	0.003	0.967
DA08a	0.02	100.16	0.839	0.631	0.768	0.036	0.011	0.953
DA08a	0.01	100.16	0.774	0.758	0.841	0.042	0.008	0.950
DA08a	0.02	100.21	0.788	0.771	0.873	0.039	0.006	0.956
DA08a	0.01	99.86	0.782	0.754	0.857	0.036	0.006	0.958
DA09	0.00	99.16	0.794	0.973	0.969	0.030	0.001	0.969
DA09	0.01	98.96	0.812	0.916	0.909	0.023	0.002	0.975
DA09	0.01	99.30	0.793	0.621	0.815	0.035	0.008	0.957
DA09	0.02	99.25	0.806	0.921	0.917	0.027	0.002	0.971
DA09	0.00	99.07	0.792	0.698	0.835	0.034	0.007	0.959
DA09	0.02	99.23	0.824	0.804	0.815	0.026	0.006	0.968
DA09	0.05	99.04	0.762	0.835	0.907	0.034	0.003	0.962

(continued)

Table 4.2 (continued)

(d)

	K_2O	Total	Mg/(Mg + Fe_2)	Fe_2/(Fetot)	Al/(Al + Fe_3 + Cr)	Jadeite	Acmite	Diopside
Pre-2011 eruption								
DA08m	0.02	99.60	0.811	0.802	0.842	0.026	0.005	0.970
DA08m	0.02	99.51	0.785	0.738	0.857	0.033	0.005	0.962
DA08m	0.00	99.81	0.809	0.780	0.827	0.032	0.007	0.962
DA08m	0.01	100.01	0.800	0.813	0.855	0.033	0.006	0.961
DA08m	0.03	100.19	0.773	0.737	0.861	0.033	0.005	0.962
DA08m	0.01	100.45	0.785	0.911	0.925	0.028	0.002	0.970

(e)

	SiO_2	TiO_2	Al_2O_3	FeO	MnO	MgO	CaO	Na_2O	K_2O	Total	X_{Ab}	X_{An}	X_{Or}
DA07	52.86	0.25	29.22	0.66	0.02	0.12	12.47	4.26	0.32	100.18	0.375	0.607	0.018
DA07	51.26	0.18	30.44	0.66	0.00	0.11	13.99	3.31	0.22	100.21	0.296	0.691	0.013
DA08a	52.27	0.23	29.98	0.70	0.00	0.12	13.03	4.02	0.25	100.63	0.353	0.633	0.014
DA09	52.06	0.24	29.37	0.69	0.01	0.12	12.96	3.90	0.35	99.69	0.345	0.634	0.020
DA09	52.30	0.23	29.46	0.73	0.01	0.09	12.86	3.83	0.29	99.80	0.344	0.639	0.017
Pre-2011 eruption													
DA08m	53.15	0.20	28.94	0.55	0.00	0.08	12.39	4.24	0.32	99.88	0.375	0.606	0.019
DA08m	53.75	0.20	29.05	0.47	0.00	0.10	11.70	4.67	0.40	100.35	0.410	0.567	0.023
DA08m	52.23	0.25	29.65	0.60	0.01	0.06	12.76	4.04	0.33	99.93	0.357	0.624	0.019
DA08m	53.31	0.23	29.09	0.52	0.00	0.09	12.09	4.43	0.38	100.15	0.390	0.588	0.022
DA08m	52.99	0.24	29.05	0.50	0.03	0.08	12.09	4.43	0.40	99.81	0.390	0.587	0.023
DA08m	54.05	0.20	28.57	0.52	0.02	0.04	11.42	4.94	0.43	100.19	0.428	0.547	0.024
DA08m	54.20	0.22	28.73	0.59	0.00	0.10	11.71	4.70	0.37	100.62	0.412	0.567	0.021
DA08m	53.53	0.21	29.46	0.51	0.00	0.09	12.32	4.44	0.39	100.99	0.386	0.592	0.022
DA08m	53.34	0.22	29.04	0.59	0.00	0.07	12.28	4.29	0.35	100.19	0.379	0.600	0.021

(f)

	DA01a	DA01b	DA02	DA08m	Lava-restingolite	Restingolite
δD%	− 89.8	− 96.4	− 96.6	− 96.3	− 87.3	− 72.2
$\delta^{18}O$%	6.2	6.1	6.2	6.4	6.8	11.1

(a) Bulk-rock (XRF) analysis (oxides in wt%; elements in ppm). (b–e) EPMA (wt%) of glass, olivine, clinopyroxene and plagioclase, respectively. (f) δD and δ18O isotope results of the Tagoro basanites and restingolite

observed results for the glass (i.e. residual liquid) and the main cotectic phases (i.e. Ol, Cpx and Pl, with total amount up to 15% for the 2011 eruption samples, and up to 30% for sample DA08m; Table 4.3). Our modelling results indicate that the assemblage olivine or clinopyroxene + plagioclase + residual glass reaches equilibrium at c. 4 kbar (i.e. c. 12 km depth assuming an average oceanic crustal density of 3000 kg/m^3), and 1130 °C, in general for all samples (Table 4.3), except for sample DA08m at slightly lower T of 1100 °C. The "silica activity barometer" of Putirka (2008, Eq. 42) for the bulk composition of sample DA08m, indicates deeper

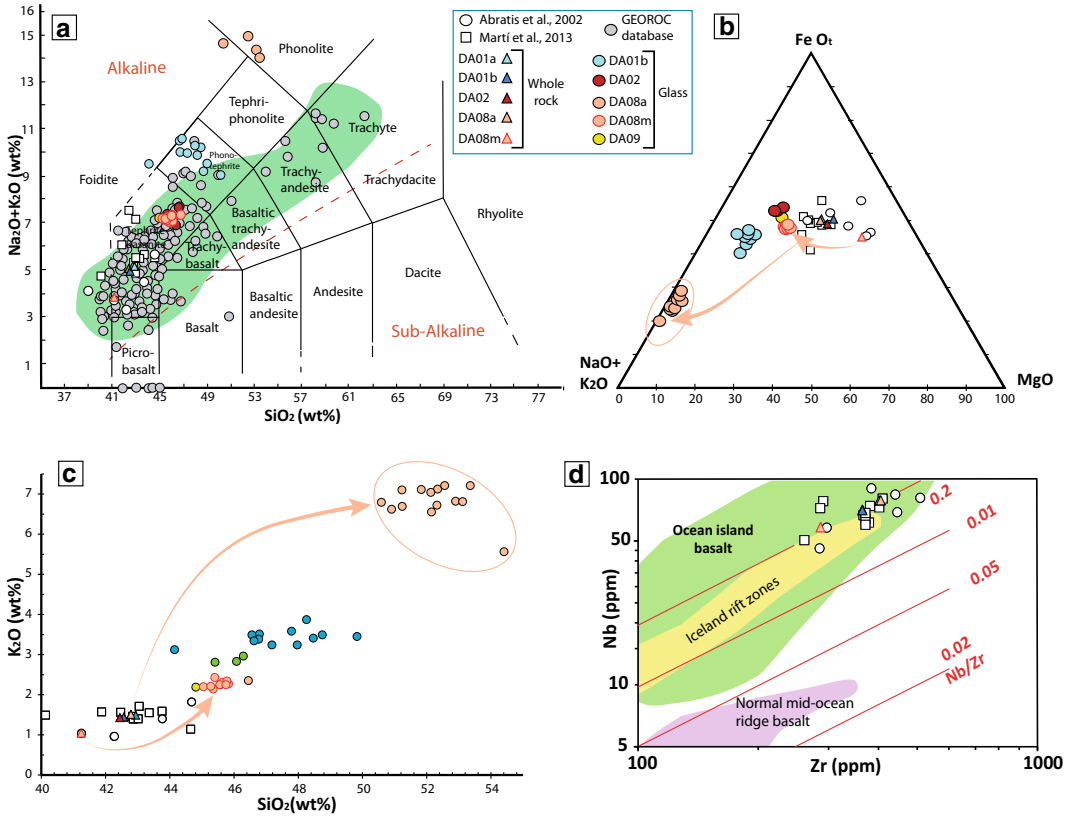

Fig. 4.3 **a** Total Alkalis versus Silica (TAS) diagram (Le Bas et al. 1986) displaying the alkaline geochemical affinity of the Tagoro rocks. Gray circles represent data for Canary Islands basanites compiled from the GEOROC database (http://georoc.mpch-mainz.gwdg.de/georoc/). The green field represents the magmatic whole-rocks of El Hierro described in Troll et al. (2012); **b** Glass compositional variation shown on a $Na_2O + K_2O$, FeOt, MgO (AFM) ternary projection (Irvine and Baragar 1971), and **c** K_2O versus SiO_2 diagram (Le Maitre 1984). Orange arrows highlight the compositional variation from the whole-rock to the glass data within the same sample; **d** Nb versus Zr comparative projection of the studied basanites with basalts from Iceland, oceanic islands and normal segments of mid-ocean ridge (Fitton and Godard 2004, for MgO > 5 wt%)

values (c. 20–24 km; López et al. 2012). The inclusion of residual glass in the thermodynamical model locally yields to inconsistent results of the output composition of the cotectic phases, as glass is equilibrating at the latest stage of cooling and might not be fully related with the first crystallised phases (i.e. Ol and/or Cpx). These results are also in line with the two main magma storage regions (10–12 and 22–36 km depth) beneath El Hierro island estimated through fluid inclusions studies (Oglialoro et al. 2017), and multifrequency, multisensor interferometric analysis of spaceborne radar images (González et al. 2013).

4.4.6 Olivine Diffusion Geospeedometry

We have acquired two compositional profiles (points every 20–30 µm) from two olivine crystals (samples DA07 and DA08m) to carry out a preliminary comparison between the 2011 early erupted products (DA07; Fig. 4.5) and the previous 2011 erupted products (DA08m; Fig. 4.6). As mentioned, olivine crystals erupted during the 2011 eruption display a variety of core and rim compositions suggesting the occurrence of multiple open-system processes before the triggering of the eruption (Martí et al. 2013b; Longpré et al.

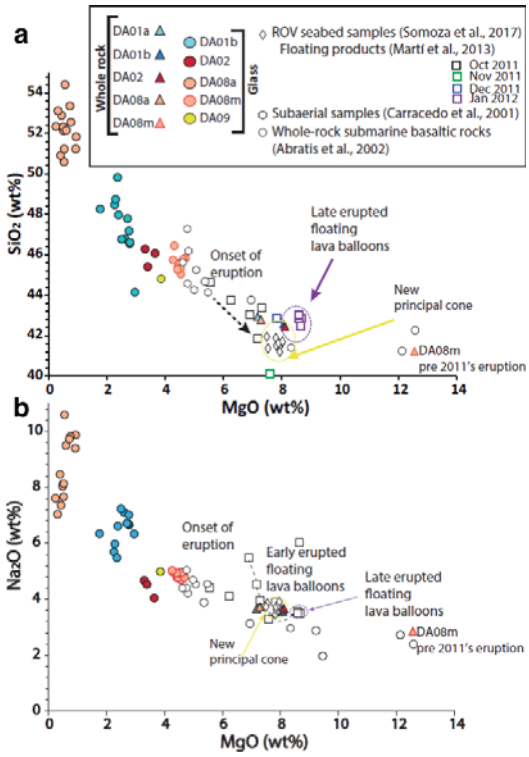

Fig. 4.4 Variation diagrams (after Somoza et al. 2017) of whole-rock major elements SiO_2 (**a**) and Na_2O (**b**) versus MgO of the studied basanites compared to other Tagoro rocks from literature (see legend). Samples DA01a and DA08a match the data for the first edifice, whereas DA02 and DA01b coincide with the last erupted products

2014). The detailed study of the olivine patterns from different eruptions is beyond the scope of this book chapter, but the comparison between these two profiles (Figs. 4.5, 4.6) highlights the importance of understanding the processes occurring at depth aiming to build a consistent model of the volcanic plumbing system.

The T and fO_2 used for modelling are 1130 ± 10 °C and 1 log units above the NNO buffer for olivine DA07, and 1100 ± 10 °C and 1 log units above the NNO buffer for olivine DA08m according to the thermobarometric results (Table 4.3). The olivine profile DA07 (Fig. 4.5) shows a reverse zoning pattern, from core to rim ($Fo_{81\text{-}84}$). Towards the crystal edge the Fo content decreases again to values of ca. Fo_{79}. However, we have established the Fo-rim value for diffusion modelling at Fo_{82} based on the slope change at this point of the transect (suggesting a last crystal-growth stage; e.g. Albert et al. (2015)). In the DA08m olivine traverse (Fig. 4.6), we also appreciate a reverse zoning trend (Fo_{78} to Fo_{82}) followed by a Fo decrease towards the edge (Fo_{80}).

We have modelled the Fe–Mg concentration gradients using the DIPRA software (Girona and Costa 2013), and have included the crystallographic directions of the compositional profiles estimated through SHAPE software (Dowty 1987). Based on these estimations, we have calculated a time of ca. 200 days for the mixing event preceding the eruption of DA08m. In the case of the 2011 sample (DA07) we have identified a mixing event occurring about 189 days followed by a resting time of 86 days prior to eruption.

4.4.7 Stable Isotopes

The results of oxygen and hydrogen stable isotope analysis (Table 4.2; Fig. 4.6) show $\delta^{18}O$ values (6.2–6.4 %) matching MORB values (5–6%) and arc volcanoes (5–8%) (Bindeman 2008). D/H results display similar values within the field of primary magmatic fluids for all samples (including the pre 2011 eruption DA08m; c. −96%). Only sample DA08a from

Table 4.3 Summary of the P–T calculations obtained for the studied basanites

	Sample		DA01a	DA01b	DA02	DA08a	DA08m
MELTS	Ol + Cpx + Glass	P (kbar)(± 0.6)	4	4	4	4	4
		T (°C) (± 40)	1130	1120	1120	1130	1100
	% residual melt; % crystals		90; 10	85; 15	85; 15	90; 10	70; 30
	Putirka (2008) Eq. 42 at 1100 °C	P (kbar)					7.0 ± 0.5

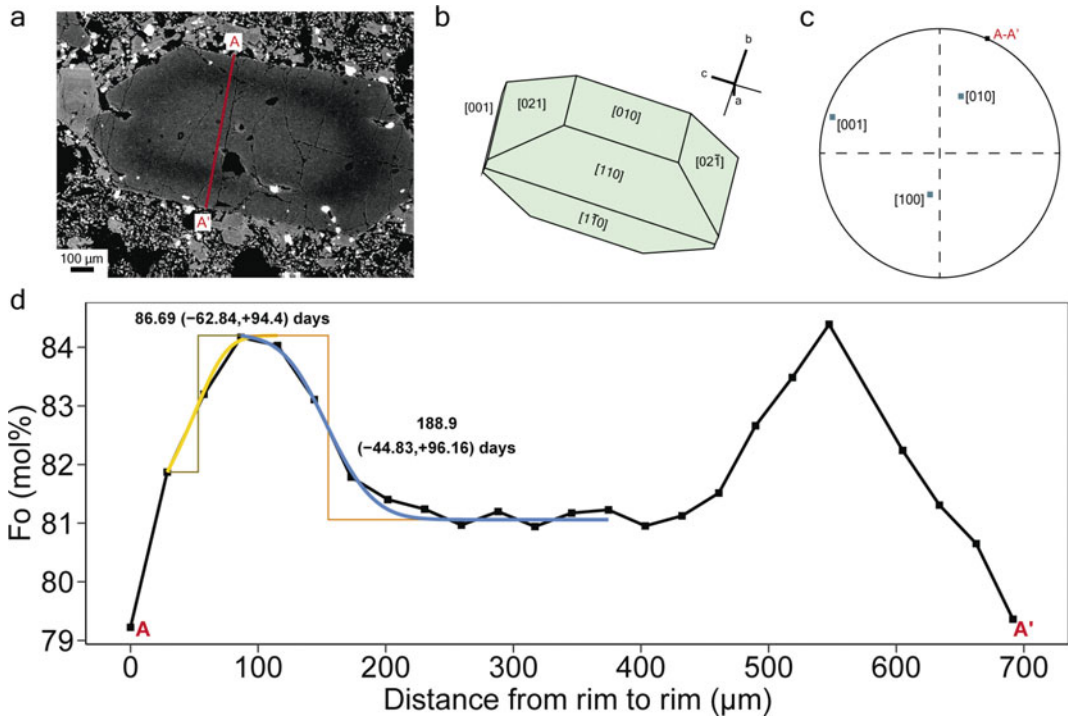

Fig. 4.5 Olivine of sample DA07. **a** Back-scattered electron (BSE) image of the crystal and position of the compositional traverse (A–A'); **b** Crystal orientation defined by SHAPE; and **c** Stereographic poles and profile orientation projection (dark green squares); **d** Olivine Fo (mol%) profile from rim to rim (A–A') and best-fit diffusion model. See the main text for the details of the calculated timescales

the earlier eruptive stage in October 2011 shows a slightly lighter value of c. −89%, which is consistent with the presence of different glass microdomains (Figs. 4.1j, 4.2i) from the magma interaction with the surrounding sediments there present prior to eruption.

Attempting to assess the potential sediments assimilation by the first products emitted in October 2011, we also analysed a white-floating sample (the so-called restingolite; e.g. Carracedo et al. 2012) and its basaltic host material. The results evidence the isotopic fractionation of the bulk values by the assimilation process of the two distinctive endmembers values. This is confirmed by the restingolite showing lighter D/H value of c. −72%, with a higher $\delta^{18}O$ value (up to 11.2%) matching the values range of sedimentary fluids (Fig. 4.6). Its host basaltic in-contact sample show also certain variation of the primary magmatic values (6.8% for $\delta^{18}O$, and −80% for D/H), which is also consistent with the major and trace elements data (Fig. 4.4, Table 4.2a–f).

4.4.8 Magnetometry

We explored whether the magnetic response represents a proxy for a magma source at depth, and it can be integrated with the rest of the petrologic and geochemical database as an informative tool of the magmatic scenario beneath Tagoro. Based on the exponential spectrum decay assumption we can estimate the depth to the top of magnetic source(s). Results show two boundaries of the magnetic anomaly (inset at Fig. 4.7): one corresponding to superficial magnetic contribution at 1 km depth, and a second one at 3 km depth. Our results match with Werner Deconvolution results. To resolve the

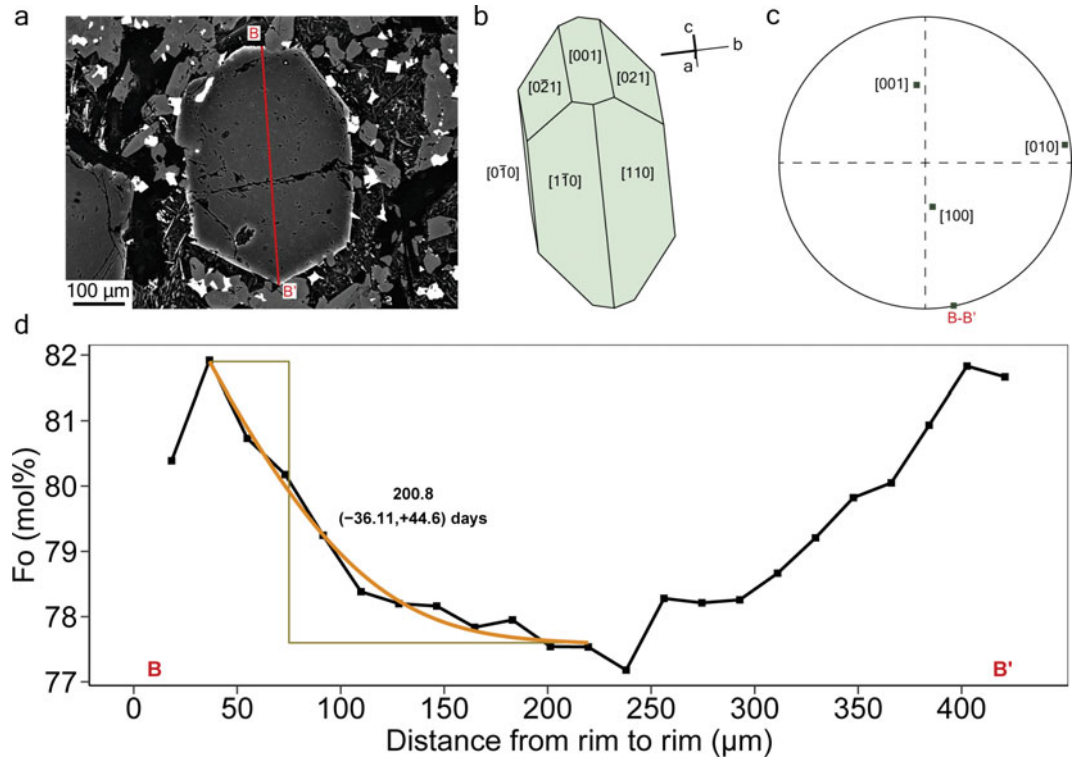

Fig. 4.6 Olivine of sample DA08m. **a** Back-scattered electron (BSE) image of the crystal and position of the compositional traverse (B–B'); **b** Crystal orientation defined by SHAPE; and **c** Stereographic poles and profile orientation projection (dark green squares); **d** Olivine Fo (mol%) profile from rim to rim (B–B') and best-fit diffusion model. See the main text for the details of the calculated timescales

depth extension of possible magnetic contributions we have used the approach proposed by Blakely (1988, 1995) and Schuey et al. (1977). Blanco-Montenegro et al. (2003) applied the method based on the position of a maximum value along the layer axis (k_{max}) to a grid centred in Gran Canaria Island, suggesting the presence of rocks located at mantle-like depths, which could behave as magnetic sources. We followed a similar technique. In order to solve the peak in the spectrum, we used 1 km as the depth of the layer's top and 10 km as depth to the Moho in the area (see also Carracedo et al. 2015). It leads to a 50 km-size for the window. Thus, using the magnetic anomaly map (Fig. 4.7) we got the radial-average spectrum of the magnetic anomaly map, and obtained a k_{max} of 0.0297 cycles/km, as well as the depth to the bottom of this magnetic source lying at 15 km b.s.l.

4.5 Discussion

4.5.1 Magmatic Evolution Up to Eruption: Mixing and Differentiation Processes

The compositional comparison (major and trace elements) between the bulk-rock (i.e. assumed as parental magma) and the evolved residual glasses (Fig. 4.3; Table 4.2) confirm the minor variation during the magmatic evolution related to the Tagoro 2011 eruption (see also Martí et al. 2013a,b). In this study we selected sample DA08m as the reference magma composition of a previous submarine eruption in the region (Álvarez-Valero et al. 2018) to be compared with the 2011–2012 products. The petrologic features

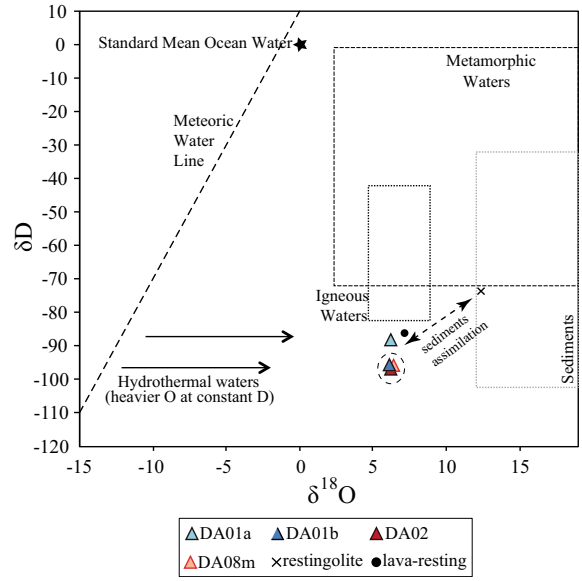

Fig. 4.7 Representation of δD versus $\delta^{18}O$ values (‰) of the Tagoro samples in Taylor's (1967) diagram of water isotopic composition (Table 4.2). The temperature of the magmas (ca. 1100°C) did not allow for oxygen equilibration or fractionation (typical at such high T) during rapid eruption, and water δD values are therefore comparable with solid samples. Isotopic variation is only evident after sediment assimilation during the first eruption period starting in October 2011

of sample DA08m with respect to the other samples erupted in 2011–2012, show (i) significantly higher MgO, Cr and Ni contents; (ii) two different P estimates of c. 24 km and c. 10–14 km depth, in line with the presence of two magma sources; and (iii) similar residence times and Fo compositional plateaus compared to the 2011–2012 samples (Longprè et al. 2014).

All this combined with the zoning patterns of the olivine crystals (Figs. 4.5, 4.6) showing mixing-derived zoning patterns (c. ≈190 and ≈90 days for the 2011–2012 eruption, and ≈200 days for the pre-2011 episode), supports the hypotheses that (i) the two submarine eruptions had similar subsurface magmatic evolution processes; and (ii) a mixing mechanism of two compositionally similar mafic magmas, one from a deeper source ascending and filling up shallower reservoirs. The deeper ascent allowed interaction between the magmabatches at c. 20–24 and 10–14 km depth. These depths range are in line with those retrieved by studies of e.g. fluid inclusions (Oglialoro et al. 2017) and geodetic (González et al. 2013). In the latter, a shallowest magma reservoir at ca. 4–5 km depth is also described, which is consistent with the depth of the reservoir's roof identified by our magnetometry survey (Fig. 4.7). The presence of two sets of olivine and pyroxene phenocrysts with and without optical undulatory extinction correlated to different deformation degrees. This in turn may be related to the two main different depths of the magmabatches; i.e. a mantle-derived source and a shallower's one, respectively (see also Longprè et al. 2014; Taracsák et al. 2019). This is also consistent with the $^{3}He/^{4}He$ results of sample DA08m with typical values of pristine magmas c. 8.7–9.7 (R_A) (Álvarez-Valero et al. 2018), whereas usually more evolved magmatic values of 2.6–5.0 (R_A) correspond to the 2011 early eruption samples DA01b and DA08a.

Therefore, this magmatic evolution is remarkable along the geological record of El Hierro, where magma mixing mechanisms at depth have characterised most of the historical eruptions on the island (e.g. Stroncik et al. 2009;

Taracsak et al. 2019). Mixing of plume-derived magmas with partial melts derived from the depleted lithospheric mantle was also described by Abratis et al. (2002) at El Hierro.

4.5.2 Connecting the Location of the Collected Samples with Their Origin at Depth: Pre-versus 2011 Eruptive Events

A key result is that the materials erupted from October 2011 until February 2012 can be related to their respective petrologic information at depth, i.e. to the rock's location on the seafloor within the Tagoro edifice. As a function of the location of the dredged samples and the geomorphological description of the Tagoro edifice (Somoza et al.2017), samples DA01a and DA08a correspond to the material forming the early volcanic edifice (i.e. October–December 2011), whereas the rest of the samples are from the last –and nowadays mostly exposed on the seafloor —edifice (January–February 2012), distributed from the summit area (DA05, DA06, DA07, DA09) up to the distal or apron parts of the lava flow (DA02 at middle of the lava flow body, and DA01b in the apron; Fig. 4.1, Table 4.1). Sample DA08m was ripped out from the pre-existing volcanic substrate (see also Stroncik et al. 2009) and collected within the same dredge of sample DA08a likely due to the dredge penetration in the thin layer of material from the first edifice at that location point (Fig. 4.1; Table 4.1).

This simple systematics between the location at surface of the 2011–2012 eruption material and their eruptive stage, as well as the common P–T estimates among all samples (i.e. same depth for the stagnated magma source) and the rest of geochemical similarities (including the isotopic data), demonstrate a fairly uninterrupted eruption episode emptying the entire plumbing system. This continuous magmatic pulse -mostly from the stagnation level- is also consistent with the seismic and deformation data supporting a partial emptying out of the deeper source as well (e.g. Martí et al. 2013a,b). Finally, the estimation of the plumbing system's volume at depth, by comparing the 2011–2012 pre- and post- eruption bathymetries, constrains a minimum volume value for the plumbing system emptying of c. 65×10^6 m^3 (Navarro 2016). This volume is higher than the previously estimated by petrological constraints (Martí et al. 2013a, b) and bathymetric maps (Rivera et al. 2013) of lower resolution than the here presented.

4.5.3 Syn-Eruption Magmatic Evolution: Eruptive Styles

Summarising the present results, a magma mixing mechanism at the stagnation level (c. 10–14 km depth) followed by a continuous eruptive event is the most plausible scenario explaining the similarities in composition of the studied samples along the whole 2011–2012 eruption period. However, three key petrographic and isotopic aspects help to constrain in more detail the syn-eruptive event. For instance, samples DA08a, belonging to the beginning of the eruption period (first edifice), is the only one revealing magma interaction with the sedimentary layers on the pre-2011 seafloor, which were heated up and partially melted by the arriving magma. This is evidenced by: (i) locally different glass microdomains in thin-section (Fig. 4.2i, j); (ii) slightly heavier bulk D/H values (Fig. 4.7); and (iii) a more evolved and fractionated geohemical composition than the rest of the samples (Fig. 4.3). The sedimentary layer was most probably fully consumed during the first edifice's building, and therefore could no longer interact with the following ascending magmas (corresponding to the rest of the studied samples) to be melted and partly assimilated. Sample DA01a, likely extracted from the first edifice as well, and compositionally identical to DA08a, shows none of the mentioned interaction features with the sediments, which may suggest that the sedimentary material had already been consumed by the time the magma corresponding to DA01a was erupted some days after 10th October 2011. The stable isotopes data reveal no interactions at the chamber or along the magma ascent to the

surface, which supports a relatively fast eruption with no isotopic re-equilibrium in the magma at high T (e.g. O'Neill 1986; Bindeman 2008; Álvarez-Valero et al. 2016, 2020), as well as an eruption mainly controlled by deep-seated processes, with little influence from shallow crustal levels (see also Longprè et al. 2014). The higher MgO content in the bulk-rock of the last erupted samples in February 2012 (DA01b, DA02, DA09) supports the removal first of the most evolved magmas (DA01a, DA08a) at the start of the eruption in October 2011 (Fig. 4.4; Table 4.2).

Given the minor variation of the MgO content in the glasses with respect to the whole-rock, we suggest a rapid emptying of the plumbing system for the 2011–2012 eruption after at least two mixing events occurred ca. six and three months prior to eruption (see also Longprè et al. 2014; Albert et al. 2016). This may be related to a deeper chamber ascent from 20–24 to 10–14 km, where a slight differentiation started because the material escape to the surface was significantly fast (c. 45 days; up to three months according to Martí et al. 2013b) (Fig. 4.8). The arrival of the deeper and more mafic pulse most likely continued until the end of the eruptive event in February 2012. This was common for the pre- 2011 eruptions as evidenced by sample DA08m and previous studies (e.g. Stroncik et al. 2009). The Fe–Mg diffusion profile in the DA07 olivine of c. a month of mafic input before the ascent (c. 15 days) and open-system eruption, strongly supports this argument (see also Longprè et al. 2014).

4.6 Conclusions

The integration of the presented new results with previous literature builds and relates the effects of the magmatic process at depth with the observations at the surface of the Tagoro area. In view of all this we conclude that the 2011–2012 eruption forming the Tagoro edifice may have followed this sequence of magmatic-volcanic stages:

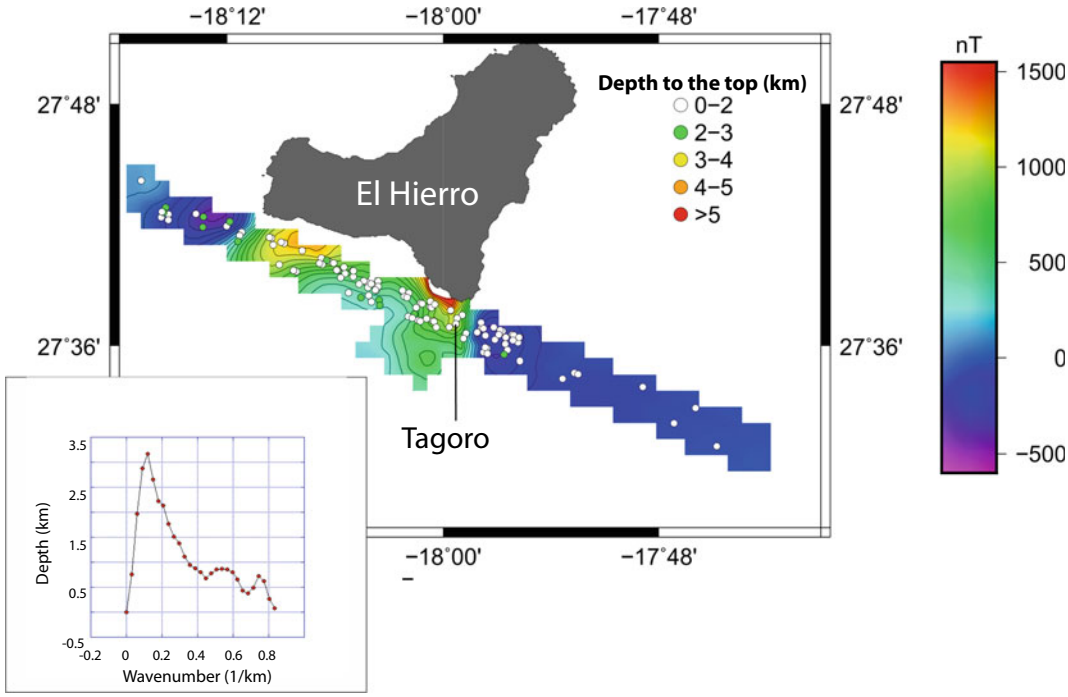

Fig. 4.8 Magnetometry map-profile and anomaly values (left-bottom corner). See the text for details

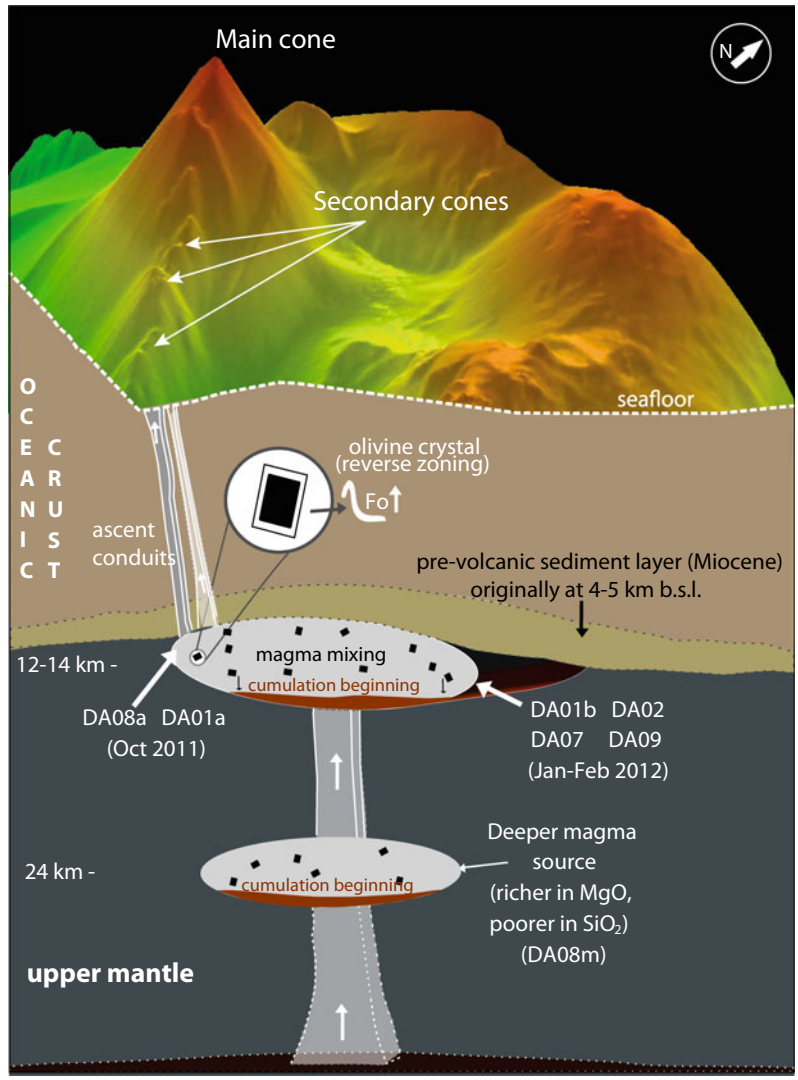

Fig. 4.9 3D summary scheme (not to scale) of the connection between the magmatic origin of the studied samples and their exposition at surface after five months of a continuous eruptive episode

(i) an original mafic magma at 20–24 km depth ascended and slightly differentiated into a shallower stagnation reservoir thus favouring mafic magma mixing (from the same magma source) by the arrival of deeper pulses that promoted instability in the latter (Fig. 4.9);

(ii) slight fractionation process (e.g. glasses of samples DA01b, DA02, DA09; Fig. 4.3) at a shallow reservoir (10–14 km depth) likely resulting in a crystal accumulation at the chamber bottom (slight higher crystallinity of sample DA09; Fig. 4.2). We are aware that the existence of small magma batches that stacked in the crust can be an alternative to a single magma chamber, which in any case managed to erupt because they mixed, increasing the volume and fracturing the crust (Albert et al. 2016);

(iii) subsequent eruption that partially or fully emptied the entire plumbing system during 4–5 months. It started erupting more massive (less vesicular) products interacting with previous seafloor sediments, which were heated and melted (and explosively emitted as part of the restingolitic material) at the beginning of the

submarine eruption in October 2011 (e.g. Carracedo et al. 2012; Pérez-Torrado et al. 2012; Troll et al. 2012; Martí et al. 2013a).

(iv) the eruption of solid material continued until February 2012 building up the last and current seafloor edifice (Somoza et al. 2017) of more vesicular material (e.g. DA01b, DA02, DA06) but nearly identical in composition along the entire eruption.

(v) the magnetometry anomaly under Tagoro retrieved in 2016 is consistent with geophysical and oceanographic evidence of post-eruptive unrest periods (Benito-Saz et al. 2019) and current activity (e.g. Fraile-Nuez et al. 2016) in the Tagoro area. This also matches the location of the Moho and shallower chamber (Carracedo et al. 2012; Martí et al. 2013a, 2013b) nowadays in the region and the entire archipelago at c. 15 km depth).

4.7 Future Work Over the Next Decade

This book opens new potential research lines to enhance the knowledge of Tagoro volcano, and volcanological processes in general. From our perspective, this chapter releases interesting new questions that can be considered as interdisciplinary action points. For instance, we are envisaging the following promising aspects to deep through in the next years: (i) exhaustive microtextural study in detail of the different glass populations combined to advanced geochemical dataset. This will allow a better understanding of the magma mixing mechanisms at depth and sediments contribution at surface; (ii) a more detailed study on diffusion chronometry in olivine, clinopyroxene and plagioclase of the pre- and 2011–2012 eruptions. As mentioned, the two olivine profiles presented here, represent just a preliminary approach to be tested with the Longprè et al. (2014) data (that does not account for the EBSD correction). Our results encourage a detailed study of the phenocryst populations in Tagoro as they show different compositional profiles (i.e. different evolution) but similar ages. This will allow us to improve our knowledge on the processes (and their timescales) preceding the monogenetic eruptions in El Hierro; (iii) a novel and timely integration of advanced geophysical techniques, such as interferometric analysis and magnetometry, with petrologic-geochemical data attempting to constrain morphologies of magma sources at depth.

All this in turn should redound in direct implications for hazard assessment and eruption forecasting in the island and at any other submarine volcanic scenario worldwide, as complementary information to the classical techniques of combining seismics, ground deformation and free-gas measurements.

Acknowledgements This research was possible thanks to: (i) the funds provided by the MINECO and FEDER through the project VULCANO I (CTM2012-36317) and the project VULCANA (Vulcana-IEO-2015-2017) funded by the Spanish Institute of Oceanography, both granted to E.F.-N., that provided the oceanographic instruments, cruise and samples; (ii) the funds provided by the MINECO and MEC grants (Spanish Government) to A. M.A.-V. through the programs EXPLORA-CIENCIA (CGL2014—61775-EXP; MINECO), José Castillejo (CAS14-00189; MEC), and Programa Propio mod. 1B—2019 (USAL). J.M. is supported by EC Grant EVE (DG ECHO H2020 826292). A.P S is grateful for his PhD grant "Programa Propio III Universidad de Salamanca, cofounded by Banco de Santander". H.A. is a Serra Húnter Lecturer Professor at the University of Barcelona. A-V specially thanks all the colleagues and friends who made possible this research starting from the ones designing the oceanographic campaigns, to those sharing their work on the vessel's deck and acoustic lab, or carrying out geochemical analysis, as well as the undergraduate and graduate students involved in the research (some developing their master and graduate theses at USAL, e.g. I.N. and N.G., respectively). We also thank the careful and in-depth reviews by D. González García, an anonymous reviewer and editor. This research is also part of the PTI VOLCAN research initiatives.

References

Abratis M, Schmincke HU, Hansteen T (2002) Composition and evolution of submarine volcanic rocks from the central and western Canary Islands. Int J Earth Sci 91:562–582

Albarede F (1992) How deep do common basaltic magmas form and differentiate? J Geophys Res 97:10997–11009

Albert H, Costa F, Martí J (2015) Timing of magmatic processes and unrest associated with mafic historical monogenetic eruptions in Tenerife Island. J Petrol 56:1945–1966

Albert H, Costa F, Martí J (2016) Years to weeks of seismic unrest and magmatic intrusions precede monogenetic eruptions. Geology 44:211–214

Albert H, Costa F, Di Muro A, Herrin J, Métrich N, Deloule E (2019) Magma interactions, crystal mush formation, timescales, and unrest during caldera collapse and lateral eruption at ocean island basaltic volcanoes (Piton de la Fournaise, La Réunion). Earth Planet Sci Lett 515:187–199

Álvarez-Valero AM, Okumura S, Arzilli F, Borrajo J, Recio CM, Ban M, Gonzalo JC, Benítez JM, Douglas M, Sasaki O, Franco P, Gómez-Barreiro J, Carnicero A (2016) Tracking bubble evolution inside a silicic dike. Lithos 262:668–676

Álvarez-Valero AM, Burgess R, Recio C, de Matos V, Sánchez-Guillamón O, Gómez-Ballesteros M, Recio G, Fraile-Nuez E, Sumino H, Flores JA, Ban M, Geyer A, Bárcena MA, Borrajo J, Compaña JM (2018) Noble gas signals in corals predict submarine volcanic eruptions. Chem Geol 480:28–34

Álvarez-Valero AM, Gisbert G, Aulinas M, Geyer A, Kereszturi G, Polo-Sánchez A, Núñez-Guerrero E, Sumino H, Borrajo J (2020) δD and $\delta^{18}O$ variations of the magmatic system beneath Deception Island volcano (Antarctica): implications for magma ascent and eruption forecasting. Chem Geol 542:119595

Asimow P, Ghiorso M (1998) Algorithmic modifications extending MELTS to calculate subsolidus phase relations. Am Mineral 83:1127–1132

Balcells R, Gomez JA (1997a) Memorias y mapas geológicos del Plan MAGNA a escala 1:25.000 de las Hojas correspondientes a la isla de El Hierro. Hoja de Frontera, Instituto Geológico y Minero de España, Spain

Balcells R, Gomez JA (1997b) Memorias y mapas geológicos del Plan MAGNA a escala 1:25.000 de las Hojas correspondientes a la isla de El Hierro. Hoja de Sabinosa, Instituto Geológico y Minero de España, Spain

Ban M, Sagawa H, Miura K, Hirotani S (2008) Evidence for a short-lived stratified magma chamber: petrology of the Z-To5 tephra layer (c. 5.8 ka) at Zao volcano, NE Japan. Geol Soc Lond Spec Publ 304(1):149–168

Becerril L, Galindo I, Martí J, Gudmundsson A (2015) Three-armed rifts or masked radial pattern of eruptive fissures? The intriguing case of El Hierro volcano (Canary Islands). Tectonophysics 647–648:33–47

Becerril L, Galve JP, Morales JM, Romero C, Sánchez N, Martí J, Galindo I (2016) Volcano-structure of El Hierro (Canary Islands). J Maps 12(1):43–52

Benito-Saz MA, Sigmundsson F, Charco M, Hooper A, Parks M (2019) Magma flow rates and temporal evolution of the 2012–2014 post-eruptive intrusions at El Hierro, Canary Islands. J Geophys Res Solid Earth 124:12576–12592

Bigeleisen J, Perlman ML, Prosser HC (1952) Conversion of hydrogenic materials to hydrogen for isotopic analysis. Anal Chem 24:1536–1537

Bindeman I (2008) Oxygen isotopes in mantle and crustal magmas as revealed by single crystal analysis. Rev Min Geochem 69:445–478

Blakely RJ (1988) Curie temperature isotherm analysis and tectonic implications of aero-magnetic data from Nevada. J Geophys Res Solid Earth 93(B10):11817–11832

Blakely RJ (1995) Potential theory in gravity and magnetic applications. Cambridge University Press, New York, p 441

Blanco-Montenegro I, Torta JM, García A, Araña V (2003) Analysis and modelling of the aeromagnetic anomalies Gran Canaria (Canary Islands). Earth Planet Sci Lett 206:601–616

Borthwick J, Harmon RS (1982) A note regarding ClF_3 as an alternative to Br $_F5$ for oxygen isotope analysis. Geochim Cosmochim Acta 46:1665–1668

Carracedo JC, Badiola ER, Guillou H, de La Nuez J, Pérez Torrado FJ (2001) Geology and volcanology of the western Canaries: La Palma and El Hierro. Estudios Geol 57:175–273

Carracedo JC, Pérez-Torrado F, Rodríguez A, Soler V, Fernández JL, Troll V, Wiesmaier S (2012) The 2011 submarine volcanic eruption in El Hierro (Canary Islands). Geol Today 28(2):53–58

Carracedo JC, Troll VR, Zaczek K, Rodríguez-González A, Soler V, Deegan FM (2015) The 2011–2012 submarine eruption off El Hierro, Canary Islands: new lessons in oceanic island growth and volcanic crisis management. Earth Sci Rev 150:168–200

Carracedo JC (2011) Geología de Canarias I (Origen, evolución, edad y vulcanismo). Ed. Rueda. Madrid

Clayton RN, Mayeda TK (1963) The use of bromine pentafluoride in the extraction of oxygen from oxides and silicates for isotopic analysis. Geochim Cosmochim Acta 27:43–52

Domínguez I, Del Fresno C, Gomis A (2014) Seismicity patterns prior to the 2011 El Hierro Eruption. Bull Seismol Soc Am 104(1):1–9

Dóniz J, Romero C, Coello E, Guillén C, Sánchez N, García-Cacho L, García A (2008) Morphological and statistical characterisation of recent mafic volcanism on Tenerife (Canary Islands, Spain). J Volcanol Geotherm Res 173:185–195

Dowty E (1987) SHAPE copyright 1994, shape software 521 Hidden Valley Road, Kingsport, TN 37663 USA. http://www.shapesoftware.com/

Fitton GJ, Godard M (2004) Origin and evolution of magmas on the Ontong Java Plateau. Geol Soc Lond Spec Publ 229:151–178

Fraile-Nuez E, González-Dávila M, Santana-Casiano JM, Arístegui J, Alonso-González IJ, Hernánez-León S, Blanco MJ, Rodríguez-Santana A, Hernández-Guerra A, Gelado-Caballero MD, Eugenio F, Marcillo J, de Armas D, Domínguez-Yanes JF, Montero MF, Laetsch DR, Vélez-Belch P, Ramos A, Ariza AV,

Cómas-Rodríguez I, Benítez-Barrios VM (2012) The submarine volcano eruption at the island of El Hierro: physical-chemical perturbation and biological response. Sci Rep 2:486

Fraile-Nuez E, Santana-Casiano JM, Vázquez JT, Gómez-Ballesteros M, Sánchez-Guillamón O, Álvarez-Valero AM, Presas-Navarro C, González-Carballo M, Castro-Álamo A, Oosterbaan M, Domínguez-Yanes JF, Herrera I (2016) VULCANA 0316 project report. http://www.repositorio.ieo.es/e-ieo/handle/10508/10035

Fraile-Nuez E, et al (2022) Ten years of intense physical-chemical, biological and geological monitoring over Tagoro submarine volcano marine ecosystem: eruptive and degassing stages. In: Chapter 8: active volcanoes of the world. Springer, Berlin, Heidelberg

Fuster JM (1993) Geochronología de la Isla de El Hierro (Islas Canarias). Bol R Soc Esp Hist Nat 88(1–4): 85–97

Ghiorso M, Sack R (1995) Chemical mass transfer in magmatic processes IV. A revised and internally consistent thermodynamic model for the interpolation and extrapolation of liquid-solid equilibria in magmatic systems at elevated temperatures and pressures. Contr Mineral Petrol 119:197–212

Girona T, Costa F (2013) DIPRA: a user-friendly program to model multi-element diffusion in olivine with applications to timescales of magmatic processes. Geochem Geophys Geosyst 14(2):422–431

Godfrey JD (1962) The deuterium content of hydrous minerals from the east-central Sierra Nevada and Yosemite National Park. Geochim Cosmochim Acta 26:1215–1245

González PJ, Samsonov S, Pepe S, Tiampo KF, Tizzani P, Casu F, Fernández J, Camacho AG, Sansosti E (2013) Magma storage and migration associated with the 2011–2012 El Hierro eruption: Implications for shallow magmatic systems at oceanic island volcanoes. J Geophys Res Solid Earth 118:4361–4377

Guillou H, Carracedo JC, Pérez Torrado F, Rodríguez Badiola E (1996) K–Ar ages and magnetic stratigraphy of a hotspot-induced, fast grown oceanic island: El Hierro, Canary Islands. J Volcanol Geotherm Res 73:141–155

Hartman RR, Teskey DJ, Friedberg JL (1971) A system for rapid digital aeromagnetic interpretation. Geophysics 36:891–918

Irvine TN, Baragar WRA (1971) A guide to the chemical classification of the common volcanic rocks. Can J Earth Sci 8:523–548

Jenkin GRT (1988) Stable isotope studies in Caledonides of SW Connemara, Ireland. PhD thesis, U. Glasgow, UK

Ku CC, Sharp JA (1983) Werner deconvolution for automated magnetic interpretation and its refinement using Marquardt's inverse modeling. Geophysics 48:754–774

Le Maitre RW (1984) A proposal by the IUGS Subcommission on the systematics of igneous rocks for a chemical classification of volcanic rocks based on the total alkali silica (TAS) diagram: (on behalf of the IUGS subcommission on the systematics of igneous rocks). Austr J Earth Sci 31(2):243–255

Le Bas M, Le Maitre R, Streckeisen A, Zanettin B (1986) A chemical classification of volcanic rocks based on the total Alkali-Silica diagram. J Petrol 27(3):745–750

Longpré MA, Klügel A, Diehl A, Stix J (2014) Mixing in mantle magma reservoirs prior to and during the 2011–2012 eruption at El Hierro, Canary Islands. Geology 42(4):315–318

Longpré MA, Stix J, Klügel A, Shimizu N (2017) Mantle to surface degassing of carbon- and sulphur-rich alkaline magma at El Hierro, Canary Islands. Earth Planet Sci Lett 460:268–280

López C, Blanco MJ, Abella R, Brenes B, Cabrera VM, Casas B, Domínguez I, Felpeto A, Fernández de Villalta M, Del Fresno C, García O, García-Arias MJ, García-Cañada L, Gomis A, González-Alonso E, Guzmán K, Iribarren I, López-Díaz R, Luengo-Oroz N, Meletlidis S, Moreno M, Moure D, Pereda de Pablo J, Rodero C, Romero E, Sainz-Maza S, Sentre MA, Torres PA, Trigo P, Villasante-Marcos V (2012) Monitoring the volcanic unrest of El Hierro (Canary Islands) before the onset of the 2011–2012 submarine eruption. Geophys Res Lett 39(L13303): 1–7

Martí J, Pinel V, López C, Geyer A, Abella R, Tárraga M, Blanco MJ, Castro A, Rodróguez C (2013a) Causes and mechanisms of the 2011–2012 El Hierro (Canary Islands) submarine eruption. J Geophys Res Solid Earth 118:823–839

Martí J, Castro A, Rodríguez C, Costa F, Carrasquilla S, Pedreira R, Bolos X (2013b) Correlation of magma evolution and geophysical monitoring during the 2011–2012 El Hierro (Canary Islands) submarine eruption. J Petrol 54(7):1349–1373

Melián G, Hernández PA, Padrón E, Pérez N, Barrancos J, Padilla G, Dionis S, Rodríguez F, Calvo D, Nolasco D (2014) Spatial and temporal variations of diffuse CO_2 degassing at El Hierro volcanic system: relation to the 2011–2012 submarine eruption. J Geophys Res Solid Earth 119:6976–6991

Navarro I (2016) Petrología y geoquímica de la evolución subvolcánica de la erupción submarina de 2011 en El Hierro (Islas Canarias). Trabajo fin de máster - Universidad de Salamanca

Nimis P (1999) Clinopyroxene geobarometry of magmatic rocks. Part 2. Structural geobarometers for basic to acid, tholeiitic and mildly alkaline magmatic systems. Contr Mineral Petrol 135:62–74

Oglialoro E, Frezzotti ML, Ferrando S, Tiraboschi C, Principe C, Gropelli G, Villa IM (2017) Lithospheric magma dynamics beneath the El Hierro volcano, Canary Islands: insights from fluid inclusions. Bull Volcanol 79:70

O'Neill JR (1986) Theoretical and experimental aspects of isotopic fractionation. In: Valley JW, Taylor, HP, O'Neil JR (eds) Stable isotopes in high temperature geological processes, MSA, vol 16, pp 1–40

Padrón E, Pérez NM, Hernández PA, Sumino H, Melián GV, Barrancos J, Nolasco D, Padilla G, Dionis S,

Rodríguez F, Hernández Í (2013) Diffusive helium emissions as a precursory sign of volcanic unrest. Geology 41(5):539–542

Paonita A, Caracausi A, Martelli M, Rizzo AL (2016) Temporal variations of helium isotopes in volcanic gases quantify pre-eruptive refill and pressurization in magma reservoirs: the Mount Etna case. Geology 44 (7):499–502

Paonita A, Liuzzo M, Salerno G, Federico C, Bonfanti P, Caracausi A, Giuffrida G, La Spina A, Caltabiano T, Gurrieri S, Giudice G (2021) Intense over pressurization at basaltic open-conduit volcanoes as inferred by geochemical signals: the case of the Mt. Etna December 2018 eruption. Sci Adv 7(36):eabg6297

Pedrazzi D, Becerril L, Martí J, Meletlidis S, Galindo I (2014) Explosive felsic volcanism on El Hierro (Canary Islands). Bull Volcanol 76:863

Pellicer MJ (1975) Estudio vulcanológico, petrológico y geoquímico de la isla de El Hierro (Archipiélago Canario). Tesis Doctoral, Facultad de Ciencias Geológicas, Universidad Complutense de Madrid, p 179

Pellicer MJ (1977) Estudio volcanológico de la Isla de El Hierro, Islas Canarias. Estud Geol 33:181–197

Pérez-Torrado FJ, Carracedo JC, Rodríguez-González A, Soler V, Troll VR, Wiesmaier S (2012) La erupción submarina de La Restinga en la isla de El Hierro, Canarias: Octubre 2011-Marzo 2012. Estud Geol 68 (1):5–27

Putirka K (2005) Igneous thermometers and barometers based on plagioclase + liquid equilibria: tests of some existing models and new calibrations. Am Mineral 90:336–346

Putirka K (2008) Thermometers and barometers for volcanic systems. Rev Mineral Geochem 69:61–120

Putirka K, Johnson M, Kinzler R, Longhi J, Walker D (1996) Thermobarometry of mafic igneous rocks based on clinopyroxene-liquid equilibria, 0–30 kbar. Contr Mineral Petrol 123(1):92–108

Rivera J, Lastras G, Canals M, Acosta J, Arrese B, Hermida N, Micallef A, Tello O, Amblas D (2013) Construction of an oceanic island: insights from the El Hierro (Canary Islands) 2011–2012 submarine volcanic eruption. Geology 41:335–358

Roeder PL, Emslie R (1970) Olivine-liquid equilibrium. Contr Mineral Petrol 29(4):275–289

Romero C (1991) Las manifestaciones volcánicas históricas del archipiélago canario, Consejería de Política Territorial, Gobierno Autónomo de Canarias, 2 tomos, Santa Cruz de Tenerife

Roubault M, Fabries J, Touret J, Weisbrod A (1963) Determination des Mineraux des Roches au Microscope Polarisant. Lamarre-Poinat, Paris, p 365

Santana-Casiano JM, González-Dávila M, Fraile-Nuez E, de Armas D, González AG, Domínguez-Yanes JF, Escánez J (2013) The natural ocean acidification and fertilization event caused by the submarine eruption of El Hierro. Sci Rep 3:1140

Santana-Casiano JM, Fraile-Nuez E, González-Dávila M, Baker ET, Resing JA, Walker SL (2016) Significant discharge of CO_2 from hydrothermalism associated with the submarine volcano of El Hierro Island. Sci Rep 6:25686

Saunders S, Blundy J, Dohmen R, Cashman K (2012) Linking petrology and seismology at an active volcano. Science 336(6084):1023–1027

Scandone R, Malone SD (1985) Magma supply, magma discharge and readjustment of the feeding system of Mount St. Helens during 1980. J Volcanol Geotherm Res 23:239–262

Sharp ZD (1990) A laser-based microanalytical method for the in situ determination of oxygen isotope ratios of silicates and oxides. Geochim Cosmochim Acta 54:1353–1357

Shuey RT, Schellinger DK, Tripp AC, Alley LB (1977) Curie depth determination from aeromagnetic spectra. Geophys J Int 50(1):75–101

Somoza L, González FJ, Barker SJ, Madureira P, Medialdea T, de Ingancio C, Lourenço N, León R, Vázquez JT, Palomino D (2017) Evolution of submarine eruptive activity during the 2011–2012 El Hierro event as documented by hydroacoustic images and remotely operated vehicle observations. Geochem Geophys Geosyst 18:3109–3137

Spector A, Grant FS (1970) Statistical model for interpretating aeromagnetic data. Geophysics 14:293–302

Stroncik NA, Klügel A, Hansteen TH (2009) The magmatic plumbing system beneath El Hierro (Canary Islands): constraints from phenocrysts and naturally quenched basaltic glasses in submarine rocks. Contr Mineral Petrol 157:593–607

Taracsák Z, Hartley ME, Burgess R, Edmonds M, Iddon F, Longprè M-A (2019) High fluxes of deep volatiles from ocean island volcanoes: Insights from El Hierro, Canary Islands. Geochim Cosmochim Acta 258:19–36

Tárraga M, Martí J, Abella R, Carniel R, López C (2014) Volcanic tremors: good indicators of change in plumbing systems during volcanic eruptions. J Volcanol Geotherm Res 273:33–40

Taylor HP (1967) Oxygen isotope studies of hydrothermalmineral deposits. In: Barnes HL (ed) Geochemistry of hydrothermal ore deposits. Holt, Rinehart and Winston, p 670

Thébault E, Finlay CC, Beggan D, Alken P, Aubert J, Barrois O, Bertrand F, Bondar T, Boness A, Brocco L, Canet E, Chambodut A, Chulliat A, Coisson P, Civet F, Du A, Fournier A, Fratter I, Gillet N, Hamilton B, Hamoudi M, Hulot G, Jager T, Korte M, Kuang W, Lalanne X, Langlais B, Léger J-M, Lesur V, Lowes FJ et al (2015) International geomagnetic reference field: the 12th generation. Earth Planets Space 57:67–79

Troll VR, Klügel A, Longpré MA, Burchardt S, Deegan FM, Carracedo JC, Wiesmaier S, Kueppers U, Dahren B, Blythe LS, Hansteen TH, Freda C, Budd DA, Jolis EM, Jonsson E, Meade FC, Harris C, Berg SE, Mancini L, Polacci M, Pedroza K (2012) Floating stones off El Hierro, Canary Islands:

xenoliths of pre-island sedimentary origin in the early products of the October 2011 eruption. Solid Earth 3:97–110

Vázquez JT, et al (2016) Preliminary geomorphological analysis of the Tagoro Volcano underwater eruption (submarine slope of El Hierro Island), Abstract Book V Simposium Internacional de Ciencias del Mar, Universidad de Alicante, Alicante, Spain

Vázquez JT, et al (2022) Geomorphological analysis of Tagoro volcanic edification along eruption and degassing phase. Chapter 7: Active Volcanoes of the World. Springer, Berlin, Heidelberg

Yamada Y, Kohno H, Murata M (1995) A low dilution fusion method for major and trace element analysis of geological samples. Adv X-Ray Anal 26:33–44